Mixtures of pollution, dust, sea salt, and volcanic aerosol during ACE-Asia: Radiative properties as a function of relative humidity

Christian M. Carrico[1]

Department of Atmospheric Science, Colorado State University, Fort Collins, Colorado, USA

Pinar Kus and Mark J. Rood

Department of Civil and Environmental Engineering, University of Illinois, Urbana, Illinois, USA

Patricia K. Quinn and Timothy S. Bates

Pacific Marine Environmental Laboratory, National Oceanic and Atmospheric Administration, Seattle, Washington, USA

[1] The *Ron Brown* cruise during ACE-Asia (March–April 2001) encountered complex aerosol that at times was dominated by marine, polluted, volcanic, and dust aerosols. Average total light scattering coefficients (σ_{sp} for $D_p < 10$ μm, relative humidity (RH) = 19%, and $\lambda = 550$ nm) ranged from 23 (marine) to 181 Mm^{-1} (dust). Aerosol hygroscopicity ranged from deliquescent with hysteresis (marine frequently and polluted variably) to hygroscopic without hysteresis (volcanic) to nearly hygrophobic (dust-dominated). Average deliquescence and crystallization RH were $77 \pm 2\%$ and $42 \pm 3\%$, respectively. The ambient aerosol was typically on the upper branch of the hysteresis loop for marine and polluted air masses and the lower branch for dust-dominated aerosols. Average f(RH = ambient), defined as σ_{sp} (RH = ambient)/σ_{sp} (RH = 19%), ranged from 1.25 (dust) to 2.88 (volcanic). Average h(RH ~60%), defined as f(RH)$_{upper\ branch}$/f(RH)$_{lower\ branch}$, were 1.6, 1.3, 1, and 1.25 for marine, polluted, volcanic, and dust, demonstrating an importance of hysteresis to optical properties. Hemispheric backscatter fraction (b) at ambient RH ranged from 0.077 (marine) to 0.111 (dust), while single scattering albedo (ω) at ambient RH ranged from 0.94 (dust and polluted) to 0.99 (marine).   *INDEX TERMS:* 0305 Atmospheric Composition and Structure: Aerosols and particles (0345, 4801); 0345 Atmospheric Composition and Structure: Pollution—urban and regional (0305); 0370 Atmospheric Composition and Structure: Volcanic effects (8409); 1610 Global Change: Atmosphere (0315, 0325); 4801 Oceanography: Biological and Chemical: Aerosols (0305); *KEYWORDS:* optical properties, radiative forcing, climate forcing, light scattering, single scattering albedo, relative humidity, mineral dust

1. Aerosols, Climate, and Air Quality in Asia

[2] As a result of population and industrialization trends, East Asia is subject to dramatically increasing atmospheric emissions from industrial and agricultural activities [*Wolf and Hidy*, 1997; *Chameides et al.*, 1999]. Additionally, dusts from the Asian deserts contribute substantially to the aerosol loading, particularly during the spring season. As this haze layer advects over the North Pacific, it interacts with marine air masses at times reaching North America [*Jaffe et al.*, 1999].

[3] Results from INDOEX portray a pervasive Indo-Asian haze layer that reduces incoming solar radiation up to 15% and extends from the Indian subcontinent into the Pacific [*Lelieveld et al.*, 2001]. The impacts of this haze layer may be large enough to influence the hydrological cycle associated with monsoon meteorology [*Ramanathan et al.*, 2001]. Though sparse, measurements even extending to rural areas of China show radiative impacts of a magnitude greater than urban areas of the United States and Europe [*Xu et al.*, 2002].

[4] Recent models and measurements demonstrate that aerosols are an important component of the global climate through their interaction with atmospheric radiation [*Kaufmann et al.*, 2002]. The "direct effect" of aerosol particles on climate involves scattering and absorption of radiation while "indirect effects" of aerosol particles, not considered here, involve aerosol influences on cloud

---

[1]Also at Department of Civil and Environmental Engineering, University of Illinois, Urbana, Illinois, USA.

properties, atmospheric stability, and chemistry. Owing to their diverse sources and atmospheric transformations, aerosol particles have a broad range of phase, composition, size, and mixing characteristics all of which affect how they interact with light.

[5] In minimizing uncertainties in aerosol climate effects, aerosol measurements in key regions are necessary to improve climate models. The Aerosol Characterization Experiment-Asia (ACE-Asia) sought to characterize the physical, chemical, optical and cloud nucleating properties of aerosols in the North Pacific Ocean and particularly the Asian outflow. As part of ACE-Asia, this study examined aerosol optical properties in the Pacific marine boundary layer and their dependencies on scanned relative humidity (RH), particle aerodynamic diameter (D_p) upper size cut, and wavelength of light (λ). These results present the first study of aerosol optical properties including the single scattering albedo (under the assumption of the RH independence of σ_{ap}) on both the upper and lower branches of the hysteresis loop and for ambient conditions for marine, polluted, mineral dust, and volcanic-influenced aerosols. These aerosol types represent important components of the climate system [Charlson et al., 1992; Sokolik and Toon, 1996; Winter and Chýlek, 1997; Robock, 2000] and are subject to complex interactions when they mix [Dentener et al., 1996; O'Dowd et al., 1997; Song and Carmichael, 2001].

2. Aerosol Radiative Properties Under Investigation

[6] Spatial and temporal heterogeneity of aerosol radiative forcing is a result of the high variability in aerosol physical and chemical properties. These properties determine the magnitude and spectral dependence of aerosol light extinction and hence climate change and visibility degradation. As appropriate, the following parameters are examined as a function of total versus backscatter, scanned RH and ambient RH, particle aerodynamic D_p upper size cut ($D_p < 10$ or 1 μm), and λ. Aerosol parameters measured here and relevant to climate forcing include the total light scattering coefficient by particles (σ_{sp}), the hemispheric backscatter coefficient (σ_{bsp}), and the light absorption coefficient (σ_{ap}).

[7] The hemispheric backscatter fraction ($b = \sigma_{bsp}/\sigma_{sp}$) is related to the upscatter fraction (β), defining the fraction of incident solar radiation scattered into space [Marshall et al., 1995]. The fraction of light scattered due to submicrometer aerodynamic diameter particles (sf) is the ratio of σ_{sp} for $D_p < 1$ μm to σ_{sp} for $D_p < 10$ μm. Distinction at $D_p < 1$ μm is useful as anthropogenic particles are primarily submicrometer D_p while natural components such as dust and sea salt are largely supermicrometer. This also often separates locally generated aerosol from those transported over long distances [Anderson and Ogren, 1998]. Single scattering albedo (ω) is determined from the ratio of σ_{sp} to σ_{ep} ($\sigma_{ep} = \sigma_{sp} + \sigma_{ap}$) and determines the atmospheric aerosols' ability to cause atmospheric cooling versus warming effects at a given surface albedo [Heintzenberg et al., 1997; Russell et al., 2002]. The Ångström exponent ($\mathring{a}$) characterizes the wavelength dependence of light scattering assuming a power law relationship of σ_{sp} and σ_{bsp} with λ [Ångström,

1964]. For discrete λ_1 and λ_2, $\mathring{a}$ is approximated by equation (1), and measurements are reported here at $\lambda = 450$ nm and 550 nm,

$$\mathring{a} \cong -\frac{\log\left(\sigma_{sp,RH,D_p,\lambda_1}/\sigma_{sp,RH,D_p,\lambda_2}\right)}{\log(\lambda_1/\lambda_2)}. \tag{1}$$

Hygroscopic properties of aerosols influence the particle size distribution and refractive index and hence radiative effects. Modeling studies have demonstrated that RH is a critical influence on aerosol climate forcing [Pilinis et al., 1995]. Particle hygroscopic growth is dependent upon composition and may range from hygrophobic to strongly hygroscopic with monotonic (smoothly varying) or deliquescent (step change) growth. For the latter, the deliquescence RH (DRH) corresponds to the equilibrium RH over an aqueous saturated solution with respect to its solute. For dry particles exposed to increasing RH, a step change in particle D_p and likewise σ_{sp} occurs at the DRH. Further increases in RH result in continued droplet growth. After deliquescence and upon exposure to decreasing RH, the aqueous droplet can form a metastable droplet, supersaturated with respect to solute concentration, until a lower crystallization RH (CRH) is attained [Tang et al., 1995; Cziczo et al., 1997; Hansson et al., 1998]. Metastable droplets exist in the atmosphere [Rood et al., 1989] and are important to climate modeling [Boucher and Anderson, 1995]. The importance of deliquescence, crystallization, and metastable droplet formation relates to whether the ambient aerosol exists in a "dry" or hydrated state. This in turn influences the radiative properties and can greatly influence the particles' role in heterogeneous aerosol chemistry [Chameides and Stelson, 1992].

[8] Aerosol hygroscopic response is described by f(RH), the ratio of σ_{sp} at a given RH to σ_{sp} at a low reference RH ($19 \pm 5\%$, where results presented as such are the arithmetic mean $\pm$ standard deviation). Likewise, f(RH) can be defined for σ_{bsp}. Results are presented as continuous functions for $35\% < RH < 85\%$ on the upper and lower branches of the hysteresis loop. Results are summarized at RH = 19%, for ambient RH, and at RH = 82% since important atmospheric aerosol species can exhibit deliquescence at RH $\leq 80\%$ [Tang and Munkelwitz, 1993]. To quantify the importance of hysteresis to radiative properties, a hysteresis factor (h(RH)) is defined as the ratio of σ_{sp} on the upper to lower branches of the hysteresis loop at a given RH.

3. Experimental Methods
3.1. Scanning Relative Humidity Nephelometry

[9] Aerosol light scattering properties were measured onboard the R/V Ronald H. Brown during ACE-Asia with scanning RH nephelometry ("humidograph") [Covert et al., 1972; Rood et al., 1989]. The instrument was described in detail by Carrico et al. [1998, 2000] but is briefly described here for clarity emphasizing a few modifications. Ambient aerosol with temperature (T) = 14.7 ± 2.4°C (arithmetic mean $\pm$ standard deviation) and RH = $72 \pm 14\%$ was sampled 18 m above sea level through a community aerosol inlet extending 5 m above and forward of the "aerosol van" on the fore deck of the 02 level. The inlet was automatically rotated into the wind to reduce particle loss and minimize

potential ship contamination [*Bates et al.*, 2002]. The lowest 1.5 m section of the mast was heated to partially dry the aerosol to a controlled RH (T = 18.9 ± 4.1°C and RH = 53 ± 4%) to ensure common sampling conditions.

[10] The aerosol stream split downstream of the community inlet into 23 tubes with 1.6 cm inner diameters from one of which the humidograph sampled at 30 actual lpm volumetric flow rate. Preceding the humidograph, Berner type inertial impactors imposed particle aerodynamic D_p upper size cuts (50% removal efficiency) of $D_p < 10$ μm (always in-line) and <1 μm (alternating in-line every other hour). In these experiments, the humidograph employed three integrating nephelometers including a pair of total scatter/backscatter three wavelength nephelometers (TSI, Inc. Model 3563 with λ = 450, 550, and 700 nm) [*Anderson et al.*, 1996] and one total scatter single wavelength nephelometer (Radiance Research Inc. (RR) Model M903 with λ = 530 nm). The RR nephelometer used a quartz-halogen flash lamp while the TSI nephelometers use a continuous quartz-halogen lamp.

[11] RH control via water vapor addition and temperature control employed a humidification system that consisted of a Teflon membrane humidifier and Peltier thermoelectric coolers (Melcor, Inc.). The humidification system preceded the second TSI and the RR nephelometers that were operated under scanning RH conditions [*Carrico et al.*, 1998, 2000; *Koloutsou-Vakakis et al.*, 2001]. The humidification system performed increasing RH scans starting from a ''dry'' aerosol state and decreasing RH scans starting from a ''hydrated'' aerosol state. This arrangement allowed examination of hysteresis and the formation of metastable droplets. The RH scans occurred over nominal one hour cycles beginning with a period at constant low RH = 38 ± 5% for 10 min, a 15 min scan to RH = 85%, a 10 min period at constant high RH = 82 ± 2%, and a 15 min scan down to RH ∼35%. To enable measurements on the upper branch of the hysteresis loop, the scan down occurred after the aerosol first achieved a local RH > 80% upstream of the scanning RH nephelometers. Additional cooling capacity enabled high local RH to be more readily achieved upstream of the RH scanning nephelometers during decreasing RH scans.

[12] RH of the scanning RH nephelometers was detected with a capacitive type RH sensor inside the TSI scanning nephelometer (described by TSI as the sample RH) and three sensors located immediately upstream of the nephelometer including a capacitive type RH sensor (Vaisala Model HMP-233) and two dew point sensors (General Eastern Inc., Models Hygro M1 and M4). Inter-calibration results from the RH sensors in an isothermal gas flow (T = 22°C) at RH = 25% and RH = 85% demonstrated agreement within 2% RH units, when comparing to a second recently factory calibrated Vaisala RH sensor (Model HMP-233 transfer standard). Dry bulb temperatures are measured with thermocouples (Omega Type K), a Pt-100 RTD temperature sensor as part of the Vaisala HMP-233, and thermistors internal to the TSI nephelometers. Inter-comparison of temperature sensors showed agreement within 0.5°C.

[13] Owing to heating by the nephelometer's lamp, RH measured upstream of the TSI nephelometer by the Vaisala RH sensor and dew point plus dry bulb sensors was greater than the nephelometer's scattering volume RH. On the basis

of the Vaisala measured RH and dry bulb temperature (using an average of a colocated thermocouple and Pt-100 RTD type sensor in the Vaisala HMP-233), dew point temperature was calculated for the Vaisala sensor. RH in the scattering volumes was calculated using this dew point temperature in conjunction with measured sample dry bulb temperatures in the RH scanning nephelometers (using the thermistor internal to the TSI nephelometers and a thermocouple with the probe tip immediately downstream of the scattering volume of the RR nephelometer). Likewise, using hygrometer measurements of dew point temperatures in conjunction with measured nephelometer sample temperatures, nephelometer scattering volume RH was calculated. An average of these four sensors was used for this analysis (Figure 1).

[14] A sample volumetric flow rate of 30 actual lpm required for impactor size cuts and to limit sample residence time combined with the desire to measure supermicrometer D_p particles necessitated the use of heating for aerosol drying. However, an important improvement from past measurements was better accounting for instrumental heating effects on sample RH and an effort to keep the sample temperature below 40°C to limit losses of semivolatile species [*ten Brink et al.*, 2000]. Maximum dry bulb temperatures were detected downstream of the preheater drier and downstream of the humidifier with average T = 39.7 ± 2.4°C and 39.3 ± 3.0°C, respectively. On the basis of 12 temperature measurements throughout the humidograph, the average sample T = 34.9 ± 4.0°C was similar to the air temperature inside the humidograph's enclosure T = 35.6 ± 1.7°C. With an aerosol residence time of ∼13 s within the humidograph, a 15% loss is expected for a pure NH_4NO_3 aerosol with a size distribution similar to ambient submicrometer diameter aerosols [*Bergin et al.*, 1997]. Substantially lower losses occurred here as the submicrometer aerosol was nss-SO_4^{2-} dominated and supermicrometer aerosol was sea salt and dust-dominated as discussed in more detail in a companion paper (P. K. Quinn et al., Aerosol optical properties measured on board the *Ronald H. Brown* during ACE-Asia as a function of aerosol chemical composition and source region, submitted to *Journal of Geophysical Research*, 2003, hereinafter referred to as Quinn et al., submitted manuscript, 2003). NO_3^- comprised <10% of the supermicrometer D_p mass and <2% of the submicrometer D_p aerosol mass.

[15] Reduced temperature gradients in the nephelometers resulted from lowering lamp power settings of the TSI nephelometers from 75W to 25W, removing the nephelometers' covers, and providing convective cooling of the nephelometers' bodies with fans. Such modifications resulted in a reduction in the temperature rise (ΔT) through the TSI nephelometer from ΔT ∼ 4.5°C to 1.7°C. This temperature gradient caused deliquescent aerosols sampled by the scanning RH nephelometers to deliquesce immediately upstream of the TSI scanning RH nephelometer where the sample achieved its highest RH. The sample RH decreased by approximately 6% (at RH = 80%) as particles entered the warmer scattering volume of the TSI scanning RH nephelometer. This caused the deliquescent step change to appear at the lower sample RH of the scanning RH nephelometer. To avoid this artifact in deliquescent humidograms presented here, f(RH) plots on the lower branch were
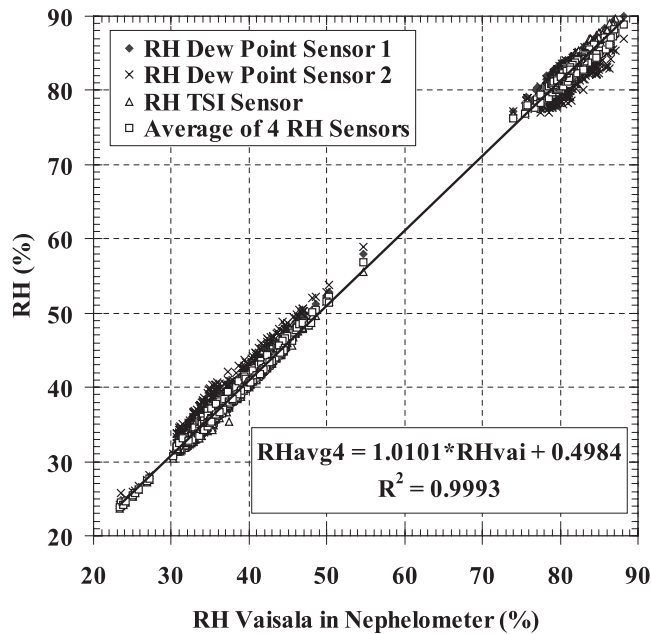
Figure 1. RH in the sample volume of the scanning RH nephelometer as measured with four sensors during periods of constant low and high RH (10 min) of each humidogram. RH measured with the Vaisala HMP-233 sensor is plotted on the x axis against RH from two dew point sensors, the RH sensor of the TSI 3563 nephelometer, and an average of all four sensors. An average of the four sensors is used for reporting these measurements.

given as a function of RH measured upstream of the TSI scanning RH nephelometer for RH < DRH. Otherwise all plots are shown as a function of nephelometers' sample volume RH. This allows proper determination of DRH and CRH values and curve fits to most accurately represent ambient aerosol behavior.

3.2. Continuous Light Scattering Measurement at Constant RH = 50 ± 8%

[16] The humidograph dried and rehydrated the aerosol to examine the RH dependence of aerosol optical properties on both the lower and upper branches of the hysteresis loop. A fourth nephelometer (TSI Inc., Model 3563) that was operated in parallel by National Oceanic and Atmospheric Administration-Pacific Marine Environmental Laboratory (NOAA-PMEL) provided continuous σ_{sp} and σ_{bsp} measurements at constant intermediate RH. By heating the sample, the aerosol only experienced decreasing RH conditions in the NOAA-PMEL nephelometer (T = 18.9 ± 4.5°C and RH = 50 ± 8%) when compared to ambient (T = 14.7 ± 2.4°C and RH = 72 ± 14%). Thus perturbation of the aerosol from its ambient hydration state by the NOAA-PMEL nephelometer was unlikely as typical ambient aerosol components would not have crystallized for such a decrease in RH as found in laboratory studies [*Tang et al.*, 1995; P. Kus et al., Evaluation between measured and modeled light scattering values for dry and hydrated laboratory aerosols, submitted to *Journal of Atmospheric and Oceanic Technology*, 2003, hereinafter referred to as Kus et al., submitted manuscript, 2003] and in the field (*Shaw and Rood* [1990] and average ambient CRH = 42 ± 3% as discussed below). Comparison of NOAA-

PMEL results with f(RH) curves obtained from the humidograph determined the ambient aerosol hydration state (i.e., on the upper branch, lower branch, or intermediate to the two branches of the hysteresis loop). With knowledge of the hydration state of the ambient aerosol, radiative properties of the ambient aerosol including f(RH = ambient) were determined from f(RH) curve fits at ambient RH. Multiplying the dry reference σ_{sp} by f(RH = ambient) in turn gives ambient σ_{sp} and σ_{bsp}.

3.3. Light Absorption and Single Scattering Albedo

[17] The light absorption coefficient (σ_{ap}) at RH $\sim$ 50% with particle aerodynamic D_p upper size cuts of D_p < 10 μm and 1 μm was derived from particle soot absorption photometer (PSAP) measurements at λ = 565 nm. The RH of the PSAP sample volume was not measured but was expected to be somewhat lower than the community inlet RH $\sim$ 55% due to heating by its light source (Quinn et al., submitted manuscript, 2003). The PSAP measured light attenuation of a filter-deposited aerosol sample to derive σ_{ap} values which were corrected for multiple scattering by the deposited aerosol and adjusted to λ = 550 nm as described by *Bond et al.* [1999]. Uncertainties may result from varying wavelength dependence of σ_{ap} for such diverse aerosol types as soot and desert dust. Aerosol single scattering albedo (ω) as a function of RH at λ = 550 nm was determined from simultaneously measured σ_{sp} (RH) and σ_{ap}, and it is assumed that σ_{ap} does not change with RH.

3.4. Calibration and Data Reduction

[18] During ACE-Asia, simultaneous calibration of the nephelometers occurred eight times (nominally every 5 days) using dry filtered air and CO_2, and zeroing of the TSI nephelometers with filtered air occurred hourly for five min. Measured T and pressure from the TSI nephelometers were used to adjust optical measurements to standard conditions of 0 °C and 1013 mbar. All light scattering measurements were corrected for nephelometer nonidealities [*Anderson and Ogren*, 1998] as a function of RH using measured values of å (RH) [*Carrico et al.*, 2000]. The same corrections were applied to the RR nephelometer with the additional adjustment from its instrumental λ = 530 nm to λ = 550 nm using measured å. For f(RH) curves, boxcar averages over 4% RH ranges were calculated and centered at every 2% RH value. Outliers beyond ±2 standard deviations of the mean values at each RH were removed from the data set. This resulted in removal of approximately 7% of the values for b and f(RH) that were based on σ_{bsp} values (the parameters with the lowest signal-to-noise ratio), and less removal of data for the other parameters.

[19] Humidograms with laboratory generated aerosols consisting of aqueous solutions containing reagent grade NaCl and $(NH_4)_2SO_4$ were examined for quality control before, during, and after the field campaign. The laboratory experiments before the field campaign also involved measurements of the particle size distribution and calculations using a Mie-Lorenz light scattering model (Kus et al., submitted manuscript, 2003). The aerosol size distribution was measured with a Scanning Differential Mobility Particle Sizing System (SMPS) that included an electrostatic classifier (TSI Model 3936 Differential Mobility Analyzer with a Model 3010-S Condensation Particle Counter). A

Mie-Lorentz light scattering code based on the "BHMIE" code of *Bohren and Huffman* [1983] was used to calculate aerosol optical properties. As necessary inputs for the Mie light scattering model, aerosol chemical properties including refractive index, density, and diameter growth factors as a function of RH were taken from *Tang* [1996]. It was assumed that particles are homogeneous spheres of uniform density for the optical calculations.

[20] On the basis of observed curve structure of the humidograms, measured f(RH) curves were fit to monotonic or deliquescent curve types. Monotonic curves feature smoothly varying f(RH) that follow similar pathways on the upper and lower branches of the hysteresis loop (equation (2)). Deliquescent curves have separate curve fits for the lower (equation (3)) and upper branches of the hysteresis loop (equation (4)) [*Kotchenruther et al.*, 1999]. The curve fit parameters a, b, c, d, and g are given in the results section for marine, polluted, volcanic and dust-dominated cases and are available in the ACE-Asia database (http://www.joss.ucar.edu/ace-asia/dm/).

$$f(RH) = 1 + a\left(\frac{RH}{100}\right)^b \quad (2)$$

$$f(RH) = \left[1 + a\left(\frac{RH}{100}\right)^b\right]$$
$$\cdot\left[1 - \frac{1}{\pi}\left(\frac{\pi}{2} + \arctan\left(1 \times 10^{24}\left\langle\frac{RH}{100} - \frac{d}{100}\right\rangle\right)\right)\right]$$
$$+ c\left(1 - \frac{RH}{100}\right)^{-g}$$
$$\cdot\left[\frac{1}{\pi}\left(\frac{\pi}{2} + \arctan\left(1 \times 10^{24}\left\langle\frac{RH}{100} - \frac{d}{100}\right\rangle\right)\right)\right] \quad (3)$$

$$f(RH) = c\left(1 - \frac{RH}{100}\right)^{-g} \quad (4)$$

4. Results and Discussion

4.1. Quality Control

[21] Of the 760 ambient humidograms generated during the cruise, 642 yielded curve fits according to equations (2)–(4). The remaining humidograms that were not included in the analyses either did not have low enough RH for a dry reference signal, had unstable RH control, or were obtained during marine time periods for D_p < 1 μm. The latter were excluded because they had too low of a signal-to-noise ratio to yield statistically significant curve fits. Among the 642 curve fits, only one showed a gross disparity (>20%) between UI and NOAA-PMEL nephelometer measurements and was discarded.

[22] A comparison of nephelometer sample RH (i.e., inside the TSI scanning RH nephelometer) for four sensors is given in Figure 1. As previously mentioned, measurements with the sensors upstream to the RH scanning nephelometers (Vaisala HMP-233 and dew point hygrometers) are adjusted based on dry bulb temperature differential to correspond to the scattering volume of the
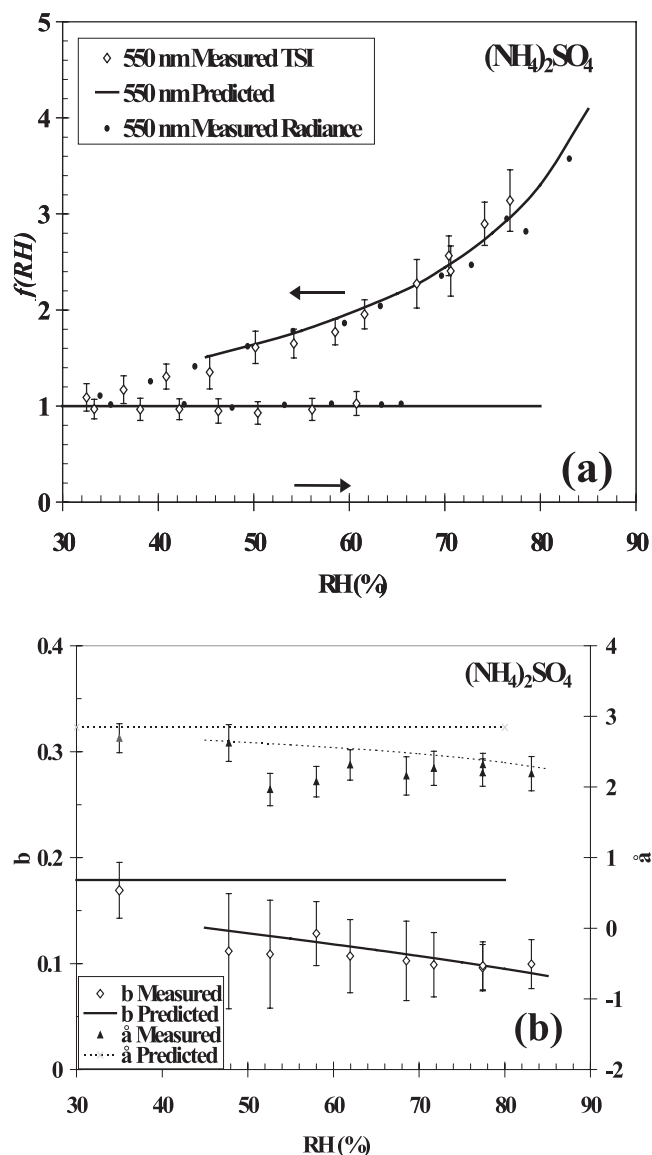
Figure 2. (NH₄)₂SO₄ laboratory generated test aerosol results for (a) fractional change in σ_{sp} as a function of RH, f(RH) and (b) hemispheric backscatter fraction, b, and Ångström exponent, å, as a function of RH. Predicted curves use Mie-Lorenz model calculations with measured size distributions (geometric mass mean D_p and standard deviation of 0.2 μm and 1.7, respectively) and physical constants from *Tang* [1996].

nephelometers. After this adjustment, RH measurements agreed within a range of 2% RH units for periods of constant high and low RH (Figure 1, Table 2).

[23] Measured and modeled values for f(RH), b, and å using submicrometer (NH₄)₂SO₄ laboratory test aerosol show agreement within ~10% (Figure 2); a complete description of test aerosol closure experiments is given by Kus et al. (submitted manuscript, 2003). Humidograms generated with NaCl and (NH₄)₂SO₄ test aerosol during the ACE-Asia field campaign exhibited DRH and CRH values of 75.2 ± 1.2% and 40.6 ± 0.8% for NaCl, and 79.0 ± 0.8% and 38.3 ± 2.1% for (NH₄)₂SO₄, respectively (Figure 3).
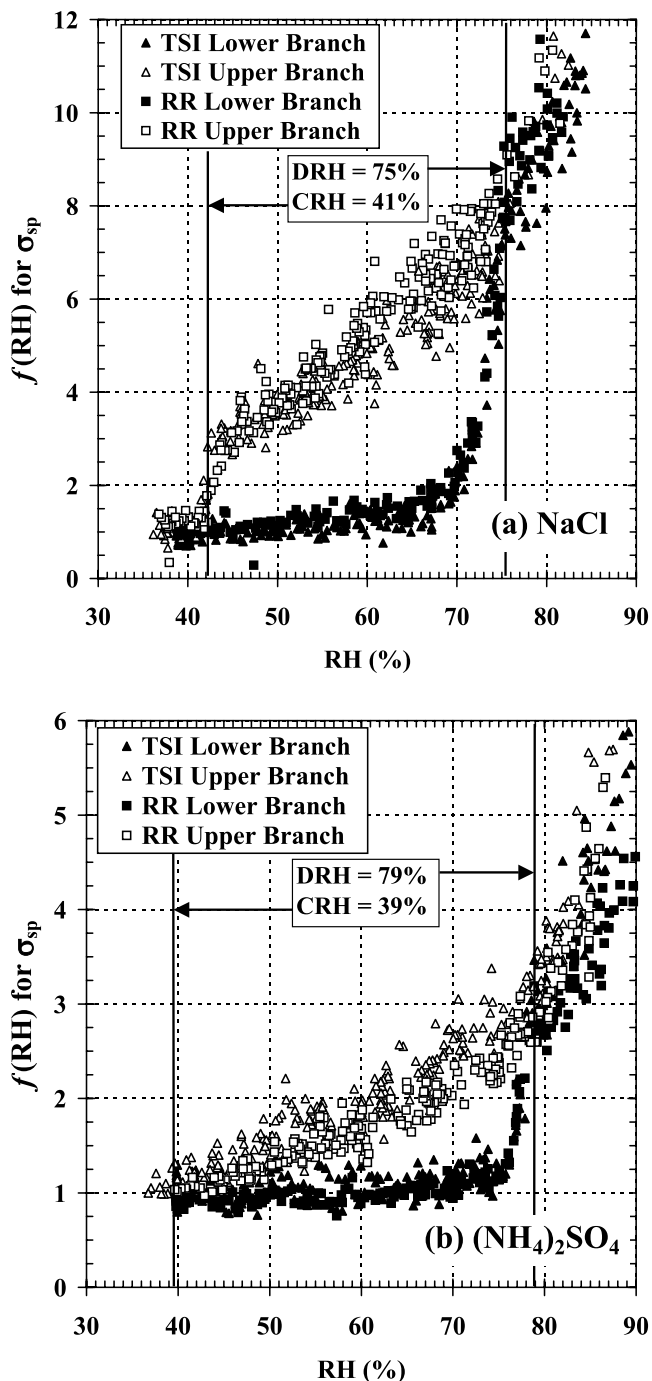
Figure 3. Measurements of f(RH) with TSI and Radiance Research (RR) instruments in the field with aerosols generated with pure salts of (a) NaCl and (b) $(NH_4)_2SO_4$. Deliquescence and crystallization RH (DRH and CRH) are the points where the lower and upper branches of the hysteresis curve intersect as shown.

Previously published values of DRH and CRH at 35 °C for NaCl are 75% and 42–43% for NaCl and 79% and 36–40% for $(NH_4)_2SO_4$, respectively [*Tang and Munkelwitz*, 1993].

[24] Owing to modest particle losses and calibration differences between the nephelometers, in particular caused by sea salt droplet impaction on the shutter of the RH scanning TSI nephelometer, σ_{sp} and σ_{bsp} measurements for the RH scanning nephelometers were normalized to agree with the upstream low RH reference nephelometer during the periods of constant low RH. Comparison of ratios of "dry" σ_{sp} values before normalization (Table 1) showed that "dry" σ_{sp} values from the RH scanning nephelometers were 4 to 8% lower than the dry reference nephelometer for $D_p < 10$ μm and 1% lower to 3% higher for $D_p < 1$ μm for all λ. Similar agreement was observed for σ_{bsp} though with more variability due to the smaller light scattering signal (~10% of σ_{sp}). During dust-dominated periods that featured a large coarse mode aerosol, the ratios were somewhat lower due to somewhat larger particle loss, particularly for the RR nephelometer (Table 1).

[25] Agreement between the NOAA-PMEL measurement of f(RH) at a relatively constant, intermediate RH with the corresponding f(RH) on the hysteresis loop was within 10%, which will be discussed later. The NOAA-PMEL measurement occurred with minimal heating from ambient T = 14.7 ± 2.4°C to sample T = 18.9 ± 4.5°C in the NOAA-PMEL nephelometer. This agreement provides strong evidence that the sample heating in the humidograph does not strongly affect the measurement of the aerosols' optical properties measured during the cruise for the aerosol types measured here. Likewise, agreement between the TSI and RR scanning RH nephelometers was within 10% for all air mass types further suggesting that instrumental differences between the nephelometers (e.g., sample heating, light source differences, truncation angles, etc.) did not cause artifacts in measurements of σ_{sp} as a function of RH.

4.2. Spatial Evolution of Aerosol Optical Properties in the North Pacific Ocean

[26] Distinct temporal evolution of aerosol optical properties is evident as the cruise sampled very diverse air masses (Figures 4 and 5, Table 3). A strong gradient in σ_{sp} is observed as the open Pacific is traversed from Hawaii to the Asian coast with 15 min average σ_{sp} ranging from as low as 4 Mm^{-1} in the most pristine marine conditions to 328 Mm^{-1} during the dust storm that brought a mixture of Gobi desert dust and

Table 1. Agreement of Light Scattering Measurements Expressed as the Ratio of the RH Scanning Nephelometer to the Dry Reference Nephelometer Signal at Low RH (Filtered for Outliers Beyond ± 2 Standard Deviations)[a]

	450 nm	550 nm	700 nm	450 nm	550 nm	700 nm	550 nm RR
All Measurements $D_p < 10$ μm							
Mean	0.96	0.95	0.92	0.99	1.01	0.93	0.94
Deviation	0.07	0.07	0.10	0.23	0.18	0.33	0.08
All Measurements $D_p < 1$ μm							
Mean	0.99	0.99	1.00	0.97	1.06	1.05	1.03
Deviation	0.09	0.09	0.24	0.55	0.30	0.87	0.07
Dust Cases $D_p < 10$ μm							
Mean	0.94	0.92	0.90	1.03	0.98	0.89	0.86
Deviation	0.03	0.02	0.04	0.10	0.07	0.09	0.05
Dust Cases $D_p < 1$ μm							
Mean	0.96	0.93	0.92	1.07	0.98	0.94	0.93
Deviation	0.06	0.03	0.07	0.16	0.07	0.19	0.05

[a]These ratios are used to normalize humidograms to begin at f(RH) = 1 at RH < 40% to account for the small particle losses and calibration differences between instruments.

Table 2. Agreement of RH Sensors Shown as Arithmetic Means and Standard Deviations at Low and High RH

	Vaisala HMP-233	General Eastern 1	General Eastern 2	TSI Model 3563	Average
Constant low RH period mean	37.4	37.8	38.6	37.3	37.8
Constant low RH period deviation	4.6	4.7	4.7	4.7	4.7
Constant high RH period mean	81.9	83.0	81.9	82.9	82.4
Constant high RH period deviation	1.9	1.8	2.0	2.0	1.9

Asian pollution. Air masses were categorized following the analysis of back-trajectories and radon as given on the *Ron Brown* air mass timeline (Web address http://saga.pmel. noaa.gov/aceasia/) and as discussed in a companion ACE-Asia paper [*Huebert et al.*, 2003]. Though at any given time the composition was a mixture of nss-SO_4^{2-}, NO_3^-, NH_4^+, and other ions, dust, sea salt, and carbon (Quinn et al., submitted manuscript, 2003), air masses were categorized as marine, anthropogenically perturbed (polluted), dust-influenced, and volcanic for these purposes (Figure 4). For these four air mass categories, a summary of the aerosol deliquescence properties is given in Table 4 while curve fit

parameters for $f(RH)$, $\omega(RH)$, $\mathring{a}(RH)$, and $b(RH)$ are given in Tables 5–8. Unless otherwise specified, all results presented here are for $D_p < 10$ μm, RH = 19 ± 5%, and $\lambda = 550$ nm.

4.2.1. Marine-Dominated Air Masses

[27]   As the ship's transect began from Hawaii on day of year (DOY) 74 (15 March 2001), unperturbed air with low-light extinction prevailed with average $\sigma_{sp} = 22 \pm 13$ Mm^{-1} (Mm^{-1} = inverse megameters) and $\sigma_{ap} = 0.5 \pm 0.3$ Mm^{-1} from DOY 74 to DOY 84 (15–25 March). The marine air masses were dominated by coarse mode particles as seen by a low submicrometer D_p fraction of light scattering ($sf = 0.31$) and low Ångström exponent ($\mathring{a} = 0.16 \pm 0.60$).
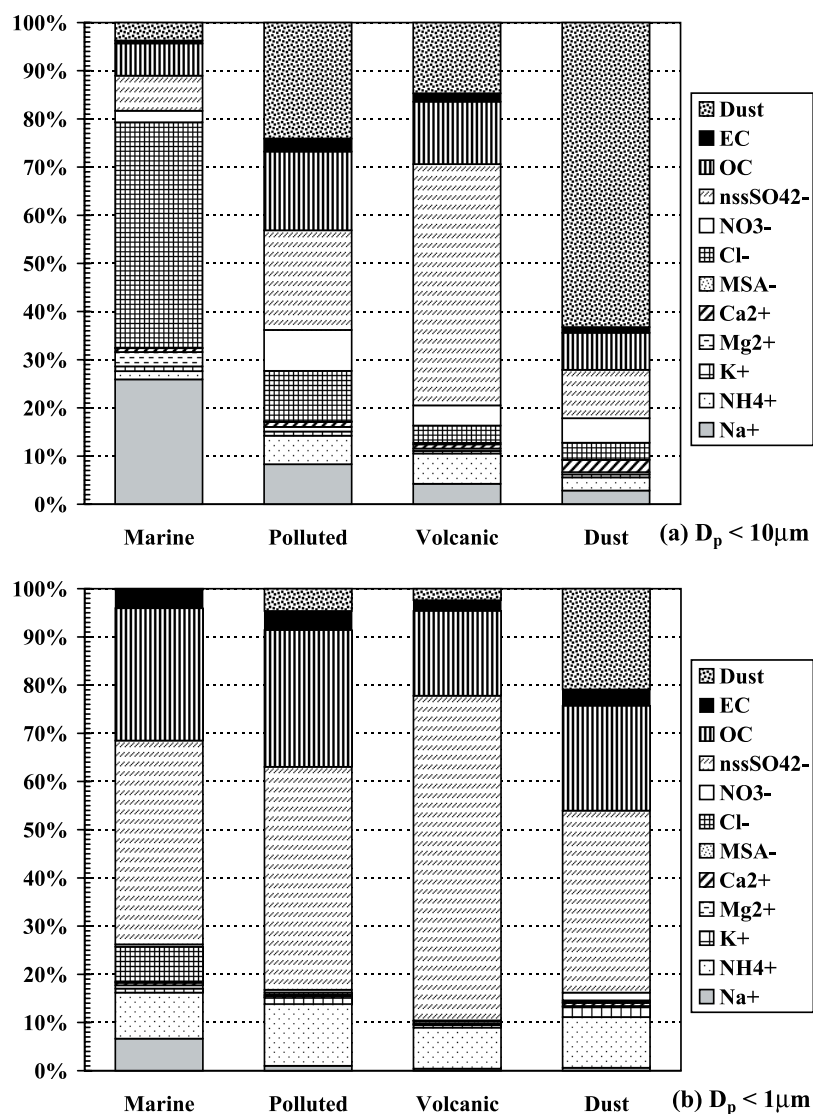
Figure 4. Summary of aerosol chemical composition of four air mass types for (a) $D_p < 10$ μm and (b) $D_p < 1$ μm.
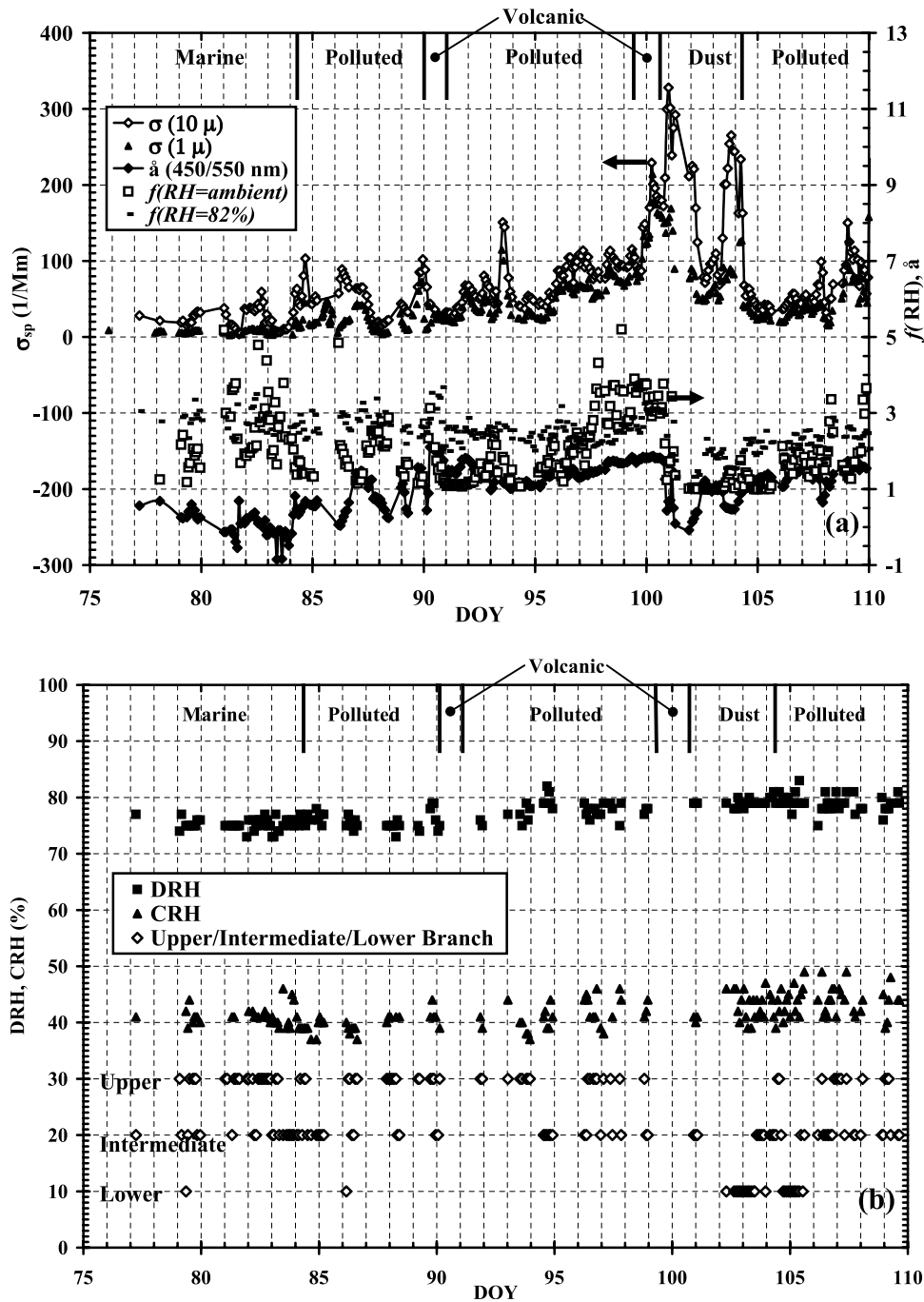
Figure 5. Time series of (a) total scattering coefficient (σ_{sp}) at $\lambda = 550$ nm and RH = $19 \pm 5\%$ and for $D_p < 10$ and 1 μm with 15 min averaging, Ångström exponent (å) at RH = 19% for $\lambda = 450$ and 550 nm, and hygroscopic growth in σ_{sp} at RH = ambient and 82% (f(RH = ambient) and f(RH = 82%)) and (b) deliquescence RH (DRH) and crystallization RH (CRH) for the deliquescent type curves for $D_p < 10$ μm during ACE-Asia (56% of measurements were deliquescent). Also shown is whether the ambient aerosol existed on the upper branch, lower branch, or intermediate to the two based on the NOAA-PMEL measurements at constant intermediate RH = $50 \pm 8\%$.

As discussed in more detail in a companion ACE-Asia paper (Quinn et al., submitted manuscript, 2003) the marine-dominated air masses contained aerosol that was predominantly sea salt for $D_p < 10$ μm and by a mixture of nss-SO$_4^{2-}$, NH$_4^+$, organic carbon, and sea salt for $D_p < 1$ μm (Figure 4).

[28] The marine aerosol demonstrated strong hygroscopicity with f(RH = 82%) = 2.45 ± 0.27 and 2.95 ± 0.39, for $D_p < 10$ μm and <1 μm, respectively. The marine aerosol showed clear evidence of deliquescence, crystallization, and hysteresis for 88% of the measurements (Figure 6). Deliquescent humidograms had DRH and CRH values of 75 ±

Table 3. Summary of Aerosol Optical Properties During ACE-Asia (at RH = 19 ± 5% and λ = 550 nm Unless Otherwise Specified) for Marine, Polluted, Volcanic, and Dust-Influenced Air Masses

	n	σ_{sp}, 1/Mm		σ_{bsp}, 1/Mm		σ_{ap},[a] 1/Mm		RH Ambient, %		ω Ambient		b Ambient		å Ambient		f(RH = Ambient)		f(RH = 82%)	
		Mean	Deviation	Mean	Deviation	Mean	Deviation	Mean	Deviation	Mean	Deviation	Mean	Deviation	Mean	Deviation	Mean	Deviation	Mean	Deviation
								D_p < 10 μm											
Marine	48	23	13	2.4	1.3	0.5	0.3	80.5	10.3	0.99	0.01	0.077	0.016	0.16	0.60	2.56	0.92	2.45	0.27
Polluted	206	64	30	7.4	3.5	6.6	4.1	71.0	13.2	0.94	0.03	0.091	0.020	1.17	0.42	1.86	0.76	2.24	0.20
Volcanic	30	114	66	12	6	8.0	2.5	82.0	13.1	0.95	0.05	0.069	0.022	1.49	0.29	2.88	0.92	2.55	0.22
Dust	32	181	82	21	8	12	6	61.3	16.5	0.94	0.02	0.111	0.019	0.74	0.34	1.25	0.48	1.69	0.25
								D_p < 1 μm											
Marine	43	7.1	2.8	0.8	0.3	0.5	0.3	76.8	11.0	0.97	0.02	–	–	1.30	0.75	2.39	0.93	2.95	0.39
Polluted	232	41	24	4.8	2.9	5.9	3.6	71.1	12.9	0.92	0.03	0.092	0.023	1.72	0.31	1.98	0.81	2.52	0.27
Volcanic	33	94	61	9.4	5.0	7.5	2.4	81.9	11.6	0.95	0.06	0.067	0.023	1.68	0.37	2.93	1.00	2.61	0.17
Dust	31	82	33	9.6	2.8	9.5	4.4	60.2	16.4	0.91	0.04	0.109	0.027	1.39	0.34	1.43	0.72	2.10	0.29

[a]Light absorption measurement performed at RH ~ 50%.

1% and 41 ± 1%, respectively, similar to laboratory measurements of sea salt aerosol [*Tang et al.*, 1997]. As a result of strong hygroscopicity, high ambient RH in the marine boundary layer (RH = 81 ± 10%), and the ambient aerosol's typical existence on the upper branch or intermediate to the two branches of the hysteresis loop (98% of measurements), a large contribution of water to ambient σ_{sp} was observed with f(RH = ambient) = 2.56 ± 0.92.

[29] Intensive aerosol parameters including ω and å had a low dependence on RH in marine air masses with å ~ 0. The marine aerosol was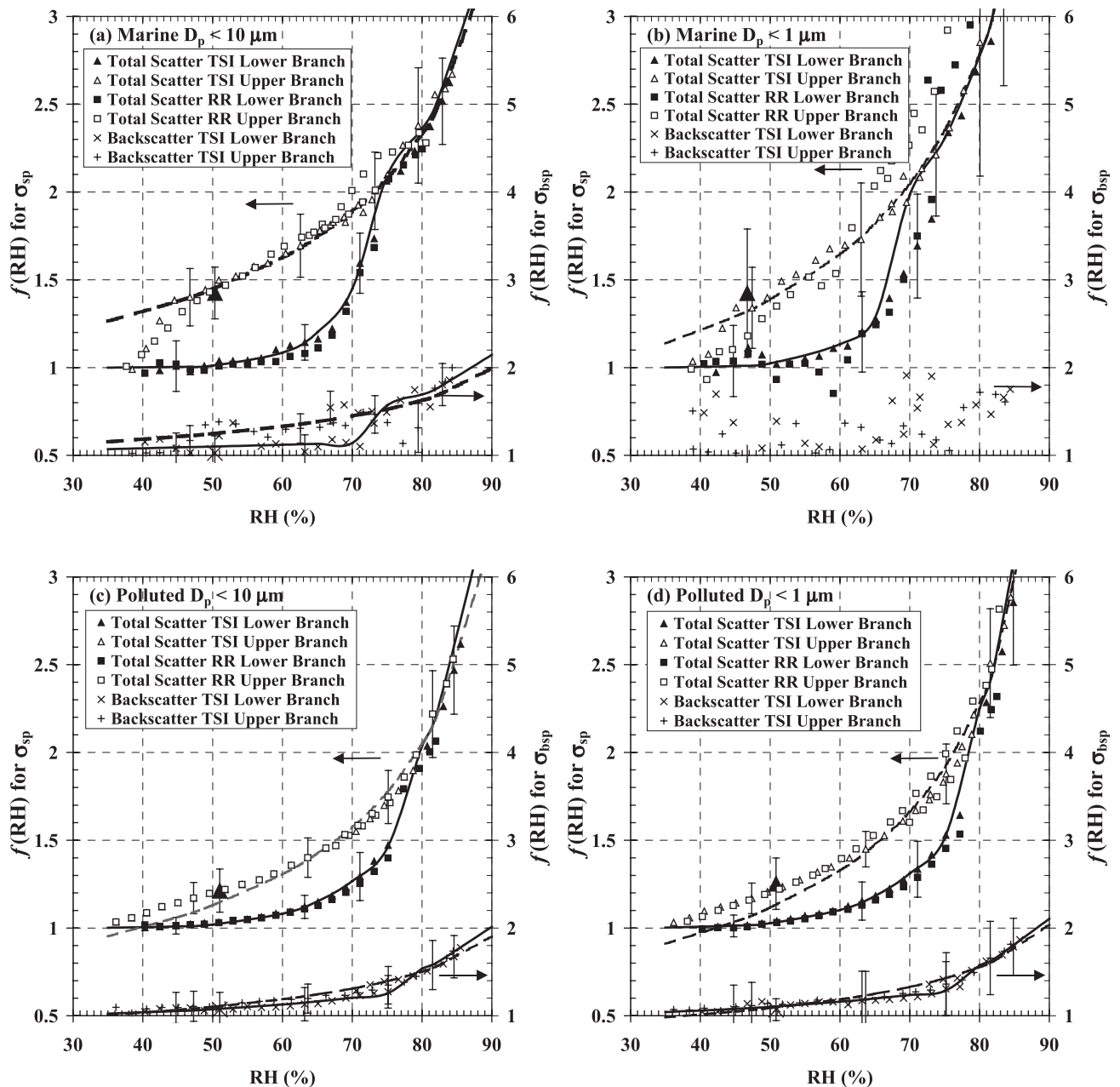 nearly a pure light scattering medium with little absorption, and thus ω was high increasing from 0.98 to 0.99 as RH increased from 40 to 85% (Figure 7). The RH dependencies of ω and å were stronger when considering aerosol with D_p < 1 μm (Figure 7). For the marine aerosol, b also demonstrated a strong dependence on RH decreasing from 0.11 at RH = 40% to 0.06 at RH = 85% (Figure 7) while b was 0.077 ± 0.016 at ambient RH. The latter has important implications to radiative forcing as β and the amount of radiation lost into space from aerosol light scattering is ultimately related to b. The marine aerosol showed the strongest influence of hysteresis with h(RH = 55%) = 1.6 (Figure 7). This indicates that f(RH) would be underestimated by 38% at RH = 55% if the ambient marine aerosol is assumed to exist on the lower branch of the hysteresis loop (i.e., modeled to exist in thermodynamic equilibrium).

4.2.2. Polluted Air Masses

[30] Although there were earlier indications of minor anthropogenic influences of the marine aerosol during DOY 81–83 (22–24 March), the influx of polluted air from Asia began in earnest on DOY 84 (25 March) at approximate coordinates 33°N, 167°E. Increases in σ_{sp}, σ_{ap}, å, and sf occurred at this time, and the hygroscopicity of the aerosol decreased slightly (Figures 5 and 6). On average, the polluted aerosol featured light extinction that was elevated substantially above background marine conditions with σ_{sp} = 64 ± 30 Mm^{-1} and σ_{ap} = 6.6 ± 4.1 Mm^{-1} (Table 3). Aerosol radiative effects were dominated by submicrometer particles with sf = 0.64 and ambient å = 1.17 ± 0.42. Polluted air masses featured conditions ranging from slightly to heavily perturbed conditions with 15 Mm^{-1} < σ_{sp} < 163 Mm^{-1} and 0.1 < σ_{ap} < 21 Mm^{-1}. Aerosol with D_p < 10 μm consisted predominately of a mixture of sea salt, dust, nss-SO_4^{2-}, NO_3-, organic carbon, and sea salt while the submicrometer D_p mass was dominated by nss-SO_4^{2-}, NH_4^+, organic carbon, and dust (Figure 4) (Quinn et al., submitted manuscript, 2003).

[31] The polluted aerosol was hygroscopic though less so than the marine aerosol with f(RH = 82%) = 2.22 ± 0.20 and 2.52 ± 0.27 for D_p < 10 μm and <1 μm, respectively (Figure 6). Polluted aerosols were deliquescent 54% of the time with DRH and CRH increasing from marine values of 75 ± 1% and 41 ± 1% to 78 ± 2% and 42 ± 3%, respectively. This was consistent with the change in aerosol composition from a sea salt dominated aerosol to one dominated by $(NH_4)_2SO_4$. With an ambient RH = 71 ± 13% the aerosol was on the upper branch or immediate to the two branches 88% of the time with f(RH = ambient) = 1.86 ± 0.76 (Table 3, Table 4).

[32] Values of ω for the polluted aerosol were lower than for marine aerosol due to the increased importance of light

Figure 6. Average hygroscopic growth in σ_{sp} and σ_{bsp} ($f(RH)\sigma_{sp}$ and $f(RH)\sigma_{bsp}$, respectively) using TSI and Radiance Research (RR) nephelometers at $\lambda = 550$ nm and for $D_p < 10$ μm and $D_p < 1$ μm for (a and b) marine, (c and d) polluted, (e and f) volcanic dominated, and (g and h) dust influenced aerosols. Curve fits for the upper (solid line) and lower (dashed line) branches of the hysteresis loop and representative standard deviations are also shown. Large symbols are mean and standard deviation from the fixed RH = 50% ± 8% NOAA-PMEL nephelometer operated in parallel to the RH scanning humidograph measurements.

absorption. There was also a stronger dependence of ω on RH with an increase from 0.91 to 0.96 as RH increased from 40% to 85% (Figure 7), and ω was 0.94 ± 0.03 at ambient RH. Also, the difference between ω on the upper and lower branches was as large as 0.02. Though å = 1.2 and was nearly constant with RH, b decreased from 0.12 to 0.09 from RH = 40% to 85% while b was 0.091 ± 0.020 at ambient RH (Table 3). The hysteresis factor h(RH = 60%) was 1.3 for the polluted aerosol, equivalent to a 23%

underestimation in f(RH = 60%) if metastable droplets are ignored.

4.2.3. Volcanic-Dominated Air Masses

[33] In the midst of the polluted period, the ship encountered volcanic plumes on DOY 90–91 (30 March) and 99.2–100.8 (9–10 April). The volcanic aerosol had elevated light extinction with $\sigma_{sp} = 114 \pm 66$ Mm^{-1} and $\sigma_{ap} = 8.0 \pm 2.5$ Mm^{-1}. Large values of sf and å ($sf = 0.83$ and å = 1.79 ± 0.21) indicated dominance by submicrometer D_p particles.
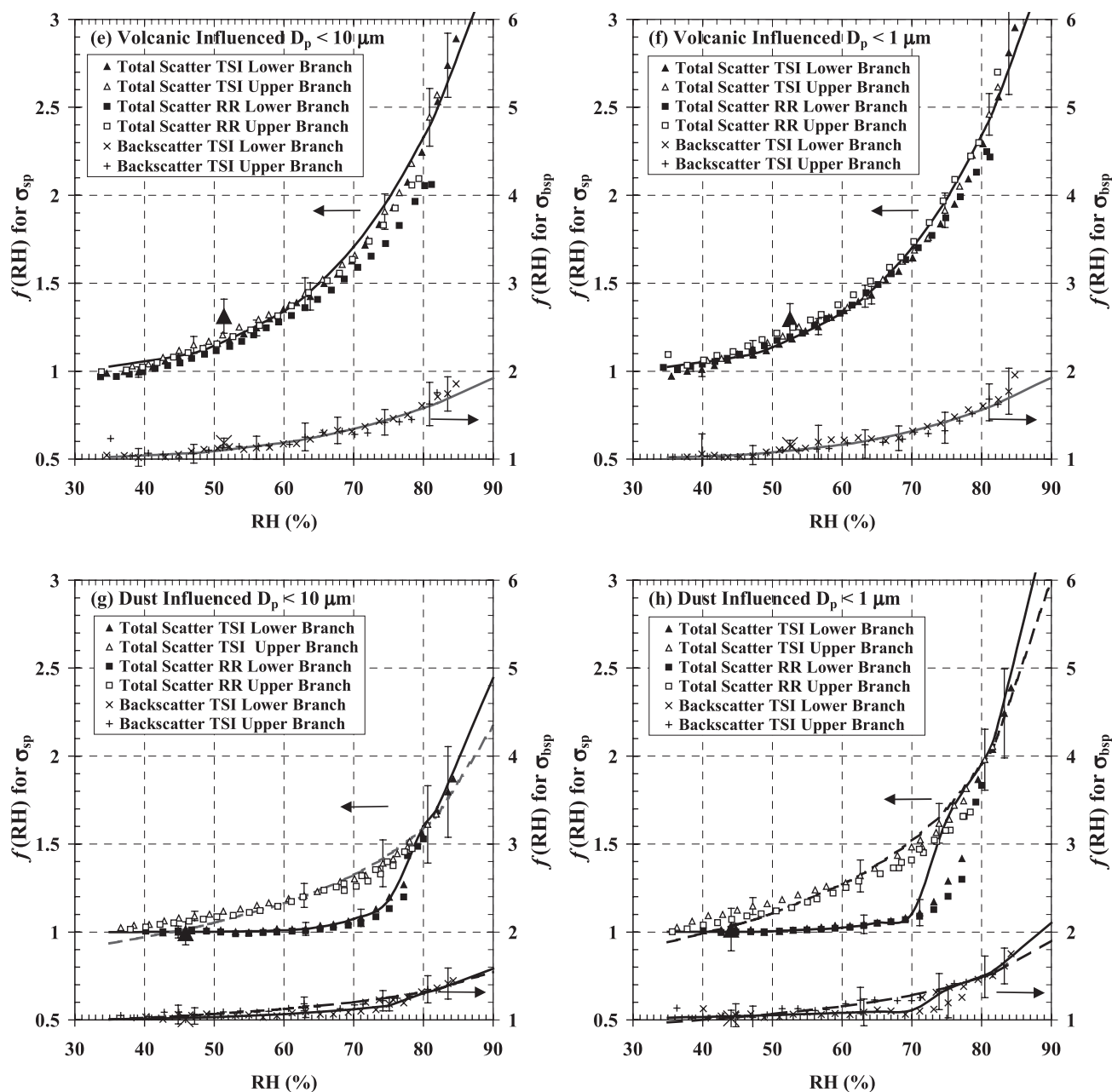
Figure 6. (continued)

The volcanic periods featured the highest "dry" σ_{sp} value for $D_p < 1$ μm reaching 215 Mm^{-1} (15 min average) on DOY 100.2 (10 April). The volcanic periods featured high SO_2 concentrations and submicrometer D_p SO_4^{2-} concentrations (reaching ~16 ppbv and 30 μg m^{-3}, respectively, on DOY 100) and a deficit in NH_4^+. Though the supermicrometer D_p aerosol was a combination of nss-SO_4^{2-}, sea salt, carbon, and NO_3^-, the prevailing submicrometer mass contribution was dominated by nss-SO_4^{2-} (Figure 4). With a deficit in NH_4^+, the nss-SO_4^{2-} is likely a mixture of H_2SO_4 and NH_4HSO_4 as discussed in more detail in a companion ACE-Asia paper [*Huebert et al.*, 2003].

[34] Volcanic aerosol showed strong hygroscopic response with $f(RH = 82\%) = 2.55 \pm 0.22$ and 2.61 ± 0.17 for $D_p < 10$ μm and <1 μm, respectively. However, little

evidence of deliquescence, crystallization, or hysteresis was observed, with $f(RH)$ following similar pathways on the upper and lower branches of the hysteresis loop (Figure 6). This was consistent with a composition showing the aerosol was only partially neutralized with the presence of H_2SO_4. There was also strong hygroscopicity with $f(RH = ambient) = 2.88 \pm 0.92$ and high RH of $82 \pm 13\%$ during the volcanic periods.

[35] The intensive aerosol parameters ω, b, and å for volcanic aerosols all demonstrated considerable RH dependencies with ω increasing from 0.91 to 0.96, b decreasing from 0.11 to 0.07, and å decreasing from 1.8 to 1.5 with RH increasing from 40% to 85%. At ambient RH, $\omega = 0.95 \pm 0.05$, $b = 0.069 \pm 0.022$, and å $= 1.49 \pm 0.29$. As a result of the smoothly varying, monotonic structure of $f(RH)$

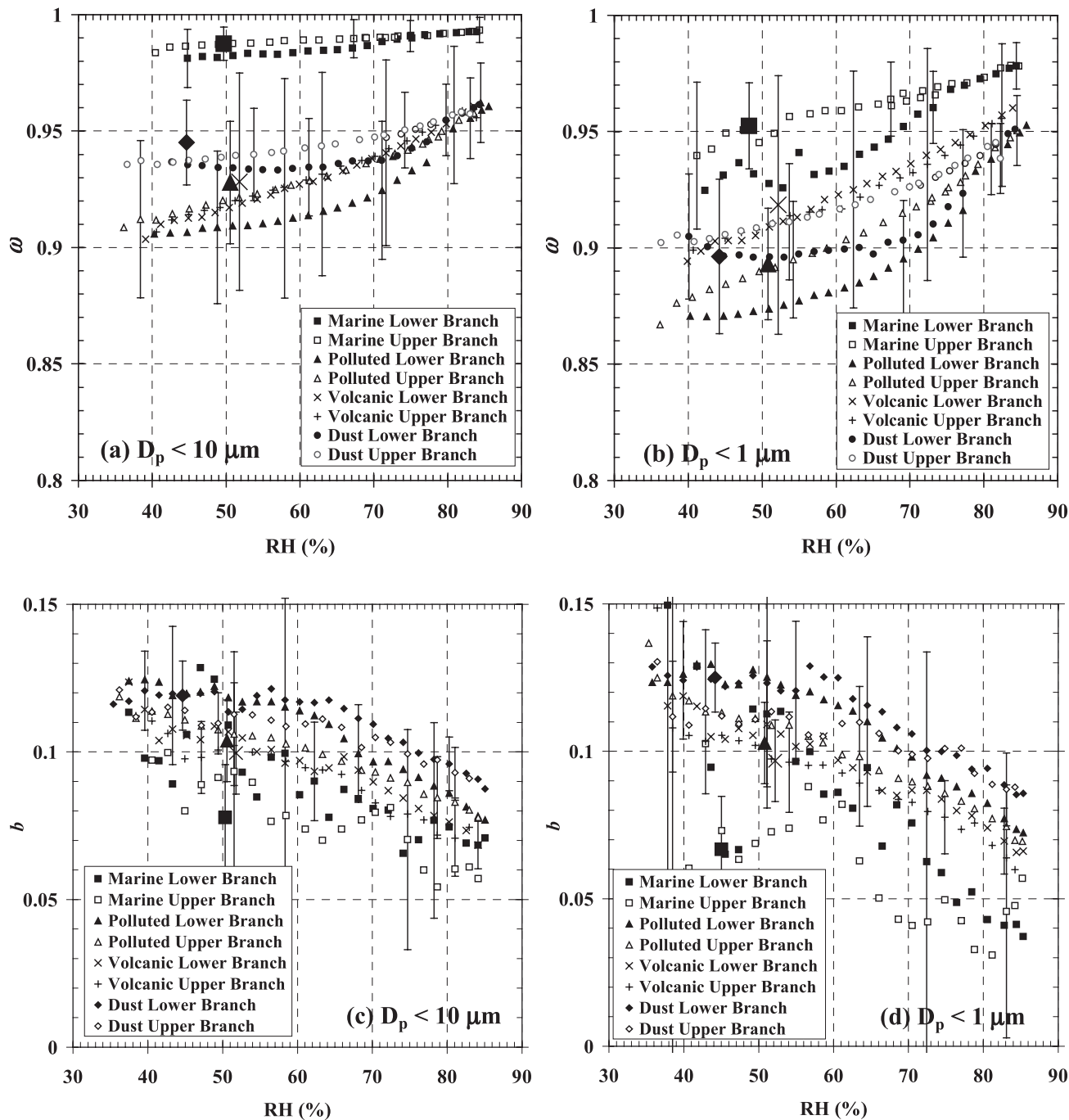**Figure 7.** RH dependence for $D_p < 10$ μm (left) and $D_p < 1$ μm (right) of (a and b) aerosol single scattering albedo (ω) at $\lambda = 550$ nm; (c and d) hemispheric backscatter fraction (b) at $\lambda = 550$ nm; (e and f) Ångström exponent (å) for wavelength pair $\lambda = 450$ and 550 nm; and (g and h) hysteresis effect ($h(RH)$) at $\lambda = 550$ nm.

(Figure 6) for volcanic aerosols, the hysteresis factor was negligible with $h(RH) \sim 1$ and approximately constant (Figure 7).

4.2.4. Dust-Influenced Air Masses

[36] Following the second volcanic period, a dramatic shift in aerosol properties occurred beginning at approximately DOY 100.8 (10 April) (Figure 5). During DOY 100.8–104.25 (10–14 April), the *Ron Brown* was under the influence of a Gobi dust-dominated aerosol arriving in the Sea of Japan (see technical appendix of *Huebert et al.* [2003]). Dust periods featured the highest average light extinction with average $\sigma_{sp} = 181 \pm 82$ Mm^{-1} and $\sigma_{ap} = 12.1 \pm 6.4$ Mm^{-1} for $D_p < 10$ μm. A shift to the predominance of supermicrometer D_p particles occurred (average $sf = 0.45$ and ambient å = 0.74 ± 0.34). During this period, the supermicrometer D_p mass was dominated by dust while the submicrometer D_p mass consisted of a combination of dust, nss-SO$_4^{2-}$, carbon and NH$_4^+$ (Figure 4).
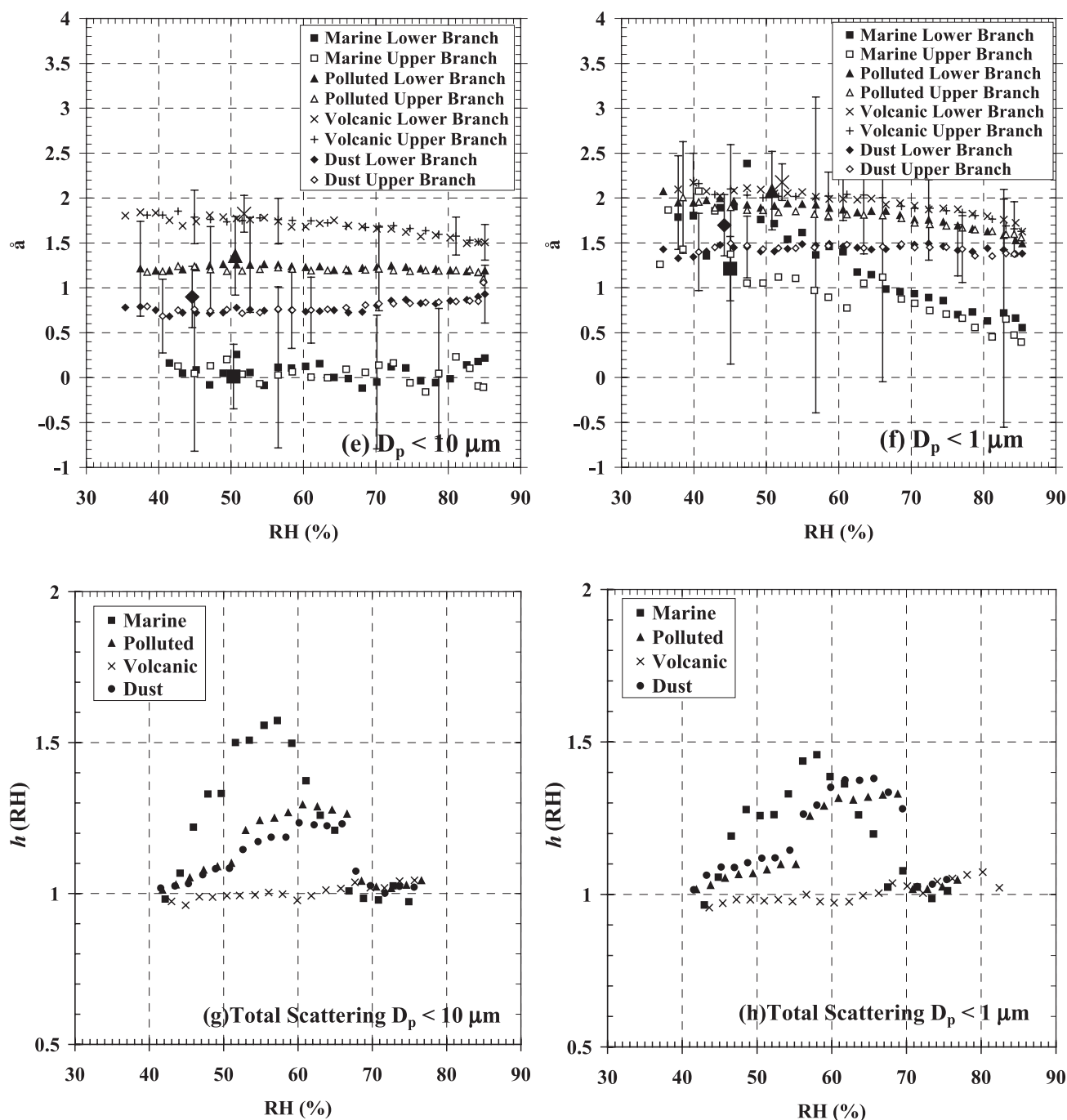
Figure 7. (continued)

[37] During the dust event, the aerosol's hygroscopic growth was substantially suppressed when compared to other periods (Figure 6). This was particularly the case for $D_p < 10$ μm aerosol but also for $D_p < 1$ μm with f(RH = 82%) = 1.69 ± 0.25 and 2.10 ± 0.29 for $D_p < 10$ μm and <1 μm, respectively. The most dust-dominated period, from approximately DOY 101.8–102.5 (11–12 April) when approximately 90% of the supermicrometer D_p mass and 50% of the submicrometer D_p mass was dust, the aerosol was nearly hydrophobic with f(RH = 82%) = 1.18 and 1.39 for $D_p < 10$ μm and <1 μm, respectively (Figure 8). Likewise, long-range transported Saharan dust

was found to be nearly hydrophobic [*Li-Jones et al.*, 1998].

[38] Despite the lower hygroscopicity, on average the dust-influenced aerosol showed strong deliquescence, crystallization and hysteretic properties (Figure 6 and 7). On average, the DRH and CRH values for the dust aerosol were 79 ± 1% and 43 ± 2%, respectively. For both $D_p < 10$ μm and <1 μm, the dust-dominated aerosol showed little growth below RH = 70% and a clear step change in f(RH) between RH = 70% and 80%. The hygroscopic behavior during dusty periods was thus likely a mixture of a nearly nonhygroscopic dust aerosol with a secondary contribution of a

Table 4. Summary of Curve Fit Type (Deliquescent or Monotonic), and for Deliquescent Cases, the Position of the NOAA-PMEL Measured σ_{sp} on the Hysteresis Loop (Upper Branch, Intermediate, Lower Branch) and Average Values of the Deliquescence (DRH) and Crystallization (CRH) Humidities for Marine, Polluted, Volcanic, and Dust-Influenced Air Masses

	Total	Monotonic		Deliquescent		Upper Branch		Intermediate		Lower Branch		DRH, %		CRH, %	
	n	n	Percent	n	Percent	n	Percent	n	Percent	n	Percent	Mean	Deviation	Mean	Deviation
$D_p < 10\ \mu m$															
Marine	48	6	12.5	42	87.5	24	60.0	15	37.5	1	2.5	75.5	1.0	41.5	1.4
Polluted	206	95	46.3	111	54.1	48	49.5	37	38.1	12	12.4	78.0	2.0	42.0	2.6
Volcanic	30	30	100.0	0	0.0	0	0.0	0	0.0	0	0.0	NA[a]	NA	NA	NA
Dust	32	8	25.0	24	75.0	0	0.0	10	41.7	14	58.3	79.3	0.6	42.8	2.0
$D_p < 1\ \mu m$															
Marine	43	27	62.8	16	37.2	16	100.0	0	0.0	0	0.0	74.1	1.3	44.0	0.6
Polluted	232	140	60.3	92	39.7	45	58.4	20	26.0	12	15.6	78.4	2.5	42.4	2.3
Dust	31	5	16.1	26	83.9	5	19.2	7	26.9	14	53.8	80.3	1.2	42.8	2.0
Volcanic	33	32	100.0	0	0.0	0	0.0	0	0.0	0	0.0	NA	NA	NA	NA

[a]NA, not applicable.

more hygroscopic population dominated by pollution and sea salt species. The mixing characteristics (i.e., internal versus external) could not be deduced from these measurements, though when present, the hygroscopic population showed deliquescence and hysteresis consistent with a neutralized inorganic aerosol.

[39] Given that the ambient aerosol was predominately on the lower branch or intermediate to the two branches of the hysteresis loop (58% and 42% of the measurements, respectively), dust-influenced aerosols often existed in a "dry" state with little water uptake until the RH was > 70%. As a result, the contribution of water to ambient σ_{sp} was relatively low with $f(\text{RH} = \text{ambient}) = 1.25 \pm 0.48$ and 1.43 ± 0.72 for $D_p < 10\ \mu m$ and $<1\ \mu m$, respectively. This was likely due to not only the lower ambient RH during the dust event (RH = $61 \pm 17\%$ versus $72 \pm 14\%$ for the cruise average), but possibly due to the RH history of the aerosol and its mineral dust chemistry.

[40] The dust air masses featured slightly higher ω values than polluted air masses with ω increasing from 0.935 to 0.96 when RH increased from 40% to 85% while $\omega = 0.94 \pm 0.02$ at ambient RH. The other aerosol intensive parameters showed RH dependencies with b decreasing from 0.12 to 0.09 and å increasing slightly from 0.8 to 0.9 when RH increased from 40% to 85%. At ambient RH b was 0.111 ± 0.019 and å was 0.74 ± 0.34. Using a Student t-test, the probability that b values were different between air masses is greater than 99% for b values at ambient RH (with the exception of the marine and volcanic comparison where the probability was 87%). The probabilities that dry b values were different between different air masses ranged from 32% to 99%. Though dry values of b were relatively similar among air masses, the RH dependency resulted in quite different b values at ambient RH conditions. As a result of the deliquescent nature of the dust-influenced aerosol, the
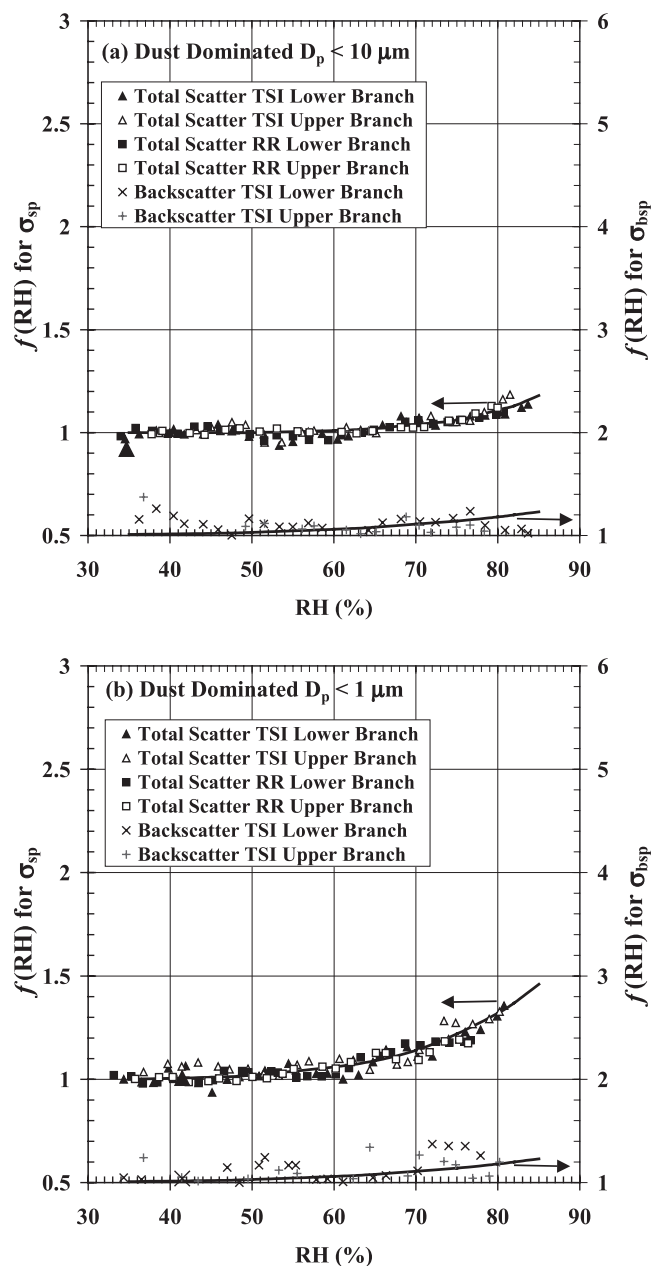

Figure 8. (opposite) Humidograms for (a) $D_p < 10\ \mu m$ and (b) $D_p < 1\ \mu m$ on approximately DOY 101.9 (11 April) during the peak of the dust event sampled on the R/V *Ronald Brown* during ACE-Asia. Large symbols are mean and standard deviation from NOAA-PMEL nephelometer operated in parallel to the RH scanning humidograph measurements.

Table 5. Curve Fit Parameters a, b, d, c, and g for Lower Branch of Hysteresis Loop Using Equation (2) (for Marine, Polluted, and Dust Cases) and a and b for Equation (4) (Volcanic Case) for $f(RH)$ for σ_{sp} and σ_{bsp}, for $\lambda = 450$, 550, and 700 nm, for Particle Diameter Upper Size Cuts of $D_p < 10$ μm and 1 μm, and for Marine, Polluted, Volcanic, and Dust-Influenced Air Masses[a]

$f(RH)_{sp}$ (10 μm, 450 nm) Lower

	a	b	d	c	g	RMSE	Conf90
Marine	11.17	9.25	71.86	0.83	0.65	0.067	0.181
Polluted	3.62	7.36	75.62	0.62	0.73	0.027	0.078
Volcanic	3.3	4.52	–	–	–	0.037	0.112
Dust	7.57	12.75	77.47	0.6	0.63	0.017	0.067

$f(RH)_{sp}$ (1 μm, 450 nm) Lower

	a	b	d	c	g	RMSE	Conf90
Marine	4.51	6.63	69.94	0.59	0.87	0.102	0.289
Polluted	3.57	7.08	77.52	0.56	0.83	0.039	0.126
Volcanic	3.32	4.65	–	–	–	0.031	0.095
Dust	2.51	8.93	73.28	0.56	0.77	0.019	0.074

$f(RH)_{bsp}$ (10 μm, 450 nm) Lower

	a	b	d	c	g	RMSE	Conf90
Marine	30.75	15	71.86	0.99	0.21	0.113	0.22
Polluted	0.92	5.24	75.62	0.78	0.37	0.03	0.069
Volcanic	1.32	4.53	–	–	–	0.058	0.09
Dust	0.19	1.55	77.47	0.57	0.57	0.111	0.401

$f(RH)_{bsp}$ (1 μm, 450 nm) Lower

	a	b	d	c	g	RMSE	Conf90
Marine	0.05	–1.81	67.94	0.77	0.35	0.197	0.376
Polluted	0.48	2.7	77.52	0.81	0.39	0.045	0.113
Volcanic	1.52	4.43	–	–	–	0.064	0.093
Dust	0.17	1.29	73.28	0.75	0.42	0.018	0.057

$f(RH)_{sp}$ (10 μm, 550 nm) Lower

	a	b	d	c	g	RMSE	Conf90
Marine	21.13	10.81	71.86	0.99	0.54	0.039	0.096
Polluted	4.17	7.7	75.62	0.59	0.77	0.028	0.083
Volcanic	3.82	4.73	–	–	–	0.043	0.137
Dust	7.61	13	77.47	0.6	0.61	0.013	0.05

$f(RH)_{sp}$ (1 μm, 550 nm) Lower

	a	b	d	c	g	RMSE	Conf90
Marine	16.16	9.4	69.94	0.73	0.83	0.065	0.199
Polluted	4.08	7.22	77.52	0.52	0.91	0.033	0.114
Volcanic	3.99	4.88	–	–	–	0.037	0.117
Dust	2.67	9.14	73.28	0.54	0.8	0.021	0.084

$f(RH)_{bsp}$ (10 μm, 550 nm) Lower

	a	b	d	c	g	RMSE	Conf90
Marine	0.2	1	71.86	0.98	0.34	0.069	0.148
Polluted	0.61	3.06	75.62	0.82	0.39	0.035	0.081
Volcanic	1.39	3.93	–	–	–	0.064	0.094
Dust	0.51	4.04	77.47	0.83	0.28	0.014	0.045

$f(RH)_{bsp}$ (1 μm, 550 nm) Lower

	a	b	d	c	g	RMSE	Conf90
Marine	0.01	–4.46	67.94	1.45	0.05	0.12	0.204
Polluted	0.58	2.52	77.52	0.8	0.42	0.039	0.1
Volcanic	1.45	4.27	–	–	–	0.061	0.093
Dust	0.24	2.16	73.28	0.68	0.49	0.028	0.091

$f(RH)_{sp}$ (10 μm, 700 nm) Lower

	a	b	d	c	g	RMSE	Conf90
Marine	26.15	11.19	71.86	1.05	0.53	0.049	0.12
Polluted	3.71	7.27	75.62	0.6	0.76	0.023	0.067
Volcanic	4	4.58	–	–	–	0.043	0.107
Dust	5.14	11.7	77.47	0.74	0.45	0.023	0.082

$f(RH)_{sp}$ (1 μm, 700 nm) Lower

	a	b	d	c	g	RMSE	Conf90
Marine	25.62	10.41	69.94	0.92	0.76	0.109	0.284
Polluted	4.77	7.27	77.52	0.49	0.99	0.062	0.223
Volcanic	5.24	5.36	–	–	–	0.07	0.25
Dust	0.86	6.03	73.28	0.53	0.79	0.028	0.112

$f(RH)_{bsp}$ (10 μm, 700 nm) Lower

	a	b	d	c	g	RMSE	Conf90
Marine	13.79	12.21	71.86	0.9	0.33	0.111	0.238
Polluted	0.99	4.44	75.62	0.89	0.36	0.027	0.062
Volcanic	1.14	3.58	–	–	–	0.064	0.088
Dust	3.91	12.86	77.47	0.68	0.39	0.043	0.146

$f(RH)_{bsp}$ (1 μm, 700 nm) Lower

	a	b	d	c	g	RMSE	Conf90
Marine	0.38	–0.97	67.94	0.64	0.59	0.16	0.414
Polluted	0.59	1	76.52	1.35	0.16	0.056	0.122
Volcanic	1.47	4.21	–	–	–	0.088	0.133
Dust	2.45	8.67	73.28	0.76	0.44	0.02	0.062

[a]Root mean square error and confidence interval at RH = 90% are also given. Measurements occurred over the range 35% < RH < 85%.

Table 6. Curve Fit Parameters c and g for the Upper Branch of Hysteresis Loop Using Equation (3) (Marine, Polluted, Dust) for f(RH) for σ_{sp} and σ_{bsp}, for λ = 450, 550, and 700 nm, for Particle Diameter Upper Size Cuts of D_p < 10 μm and 1 μm, and for Marine, Polluted, Volcanic, and Dust-Influenced Air Masses[a]

	f(RH)$_{sp}$ (10 μm, 450 nm)				f(RH)$_{sp}$ (10 μm, 550 nm)				f(RH)$_{sp}$ (10 μm, 700 nm)			
	c	g	RMSE	Conf90	c	g	RMSE	Conf90	c	g	RMSE	Conf90
Marine	0.93	0.58	0.073	0.137	1.01	0.52	0.038	0.068	1.08	0.51	0.05	0.088
Polluted	0.73	0.64	0.05	0.088	0.72	0.65	0.055	0.099	0.73	0.64	0.056	0.099
Volcanic	–	–	–	–	–	–	–	–	–	–	–	–
Dust	0.77	0.47	0.039	0.076	0.77	0.45	0.039	0.074	0.8	0.4	0.039	0.072
	f(RH)$_{sp}$ (1 μm, 450 nm)				f(RH)$_{sp}$ (1 μm, 550 nm)				f(RH)$_{sp}$ (1 μm, 700 nm)			
	c	g	RMSE	Conf90	c	g	RMSE	Conf90	c	g	RMSE	Conf90
Marine	0.71	0.76	0.131	0.273	0.82	0.76	0.076	0.174	1.05	0.69	0.194	0.383
Polluted	0.67	0.72	0.062	0.118	0.65	0.78	0.067	0.133	0.63	0.84	0.096	0.201
Volcanic	–	–	–	–	–	–	–	–	–	–	–	–
Dust	0.73	0.6	0.048	0.108	0.72	0.62	0.052	0.118	0.71	0.61	0.06	0.135
	f(RH)$_{bsp}$ (10 μm, 450 nm)				f(RH)$_{bsp}$ (10 μm, 550 nm)				f(RH)$_{bsp}$ (10 μm, 700 nm)			
	c	g	RMSE	Conf90	c	g	RMSE	Conf90	c	g	RMSE	Conf90
Marine	0.94	0.24	0.051	0.072	1.02	0.29	0.095	0.139	0.75	0.47	0.15	0.257
Polluted	0.82	0.33	0.051	0.072	0.87	0.34	0.054	0.077	0.87	0.36	0.065	0.094
Volcanic	–	–	–	–	–	–	–	–	–	–	–	–
Dust	0.88	0.27	0.061	0.096	0.91	0.23	0.028	0.044	0.87	0.24	0.035	0.056
	f(RH)$_{bsp}$ (1 μm, 450 nm)				f(RH)$_{bsp}$ (1 μm, 550 nm)				f(RH)$_{bsp}$ (1 μm, 700 nm)			
	c	g	RMSE	Conf90	c	g	RMSE	Conf90	c	g	RMSE	Conf90
Marine	0.9	0.24	0.176	0.246	0.85	0.37	0.131	0.22	0.9	0.34	0.165	0.27
Polluted	0.82	0.37	0.059	0.087	0.83	0.39	0.065	0.097	0.96	0.36	0.079	0.116
Volcanic	–	–	–	–	–	–	–	–	–	–	–	–
Dust	0.84	0.33	0.049	0.082	0.83	0.36	0.047	0.086	0.84	0.36	0.056	0.102

[a]Root mean square error and confidence interval at RH = 90% are also given. Volcanic case follows the same parameters as given in Table 5. Measurements occurred over the range 35% < RH < 85%.

hysteresis factor was substantial with h(RH = 60%) = 1.25 (Figure 7).

5.   Summary and Conclusions

[41]   Complex mixtures of marine, polluted, desert dust, and volcanic aerosols were characterized on the R/V *Ronald H. Brown* during ACE-Asia from DOY 74–110 (15 March through 20 April 2001). These results are the first comprehensive measurements of climate relevant aerosol optical properties on both the upper and lower branches of the hysteresis loop and for ambient RH for such complex mixtures. The scanning relative humidity (RH) nephelometery system measured light scattering and backscattering coefficients (σ_{sp} and σ_{bsp}) as a function of RH, wavelength of light (λ), and aerodynamic particle diameter upper size cut (D_p < 10 and <1 μm). Curves of light scattering values versus RH (f(RH)) were classified based on air mass type and fit as either smooth monotonic or deliquescent functions. Ambient aerosol hydration state was investigated and has important implications to particle phase, composition, size and shape and thus radiative forcing, visibility impacts, and heterogeneous atmospheric chemistry.

[42]   During the first 10 days of the cruise beginning in Hawaii on DOY 74 (15 March 2001), unperturbed marine air masses predominated with σ_{sp} = 23 ± 13 Mm^{-1}, σ_{ap} = 0.5 ± 0.3 Mm^{-1} (RH = 19% and 55%, respectively, and D_p < 10 μm and λ = 550 nm) and were dominated by coarse sea salt particles (fraction of scattering by submicrometer D_p particles sf = 0.31). Marine cases featured strong hygroscopicity and showed clear evidence of deliquescence and hysteresis. Approaching the Asian coast, anthropogenically

perturbed air masses arrived having higher light extinction of σ_{sp} = 64 ± 30 Mm^{-1}, σ_{ap} = 6.6 ± 4.4 Mm^{-1}, and a strong submicrometer contribution to σ_{sp} (sf = 0.68). Pollution-dominated aerosols were somewhat less hygroscopic than marine aerosols and demonstrated a wider range of deliquescent and smoothly monotonic growth properties. Volcanic-influenced aerosols featured yet higher light extinction with σ_{sp} = 114 ± 66 Mm^{-1} and σ_{ap} = 11.7 ± 5.6 Mm^{-1} and were dominated by submicrometer particles (sf = 0.83). Volcanic-dominated aerosols were strongly hygroscopic and featured smoothly monotonic growth as a result of their acidic nature. Dust-dominated aerosols during the period from DOY 101 to 104 (11 to 14 April) exhibited the highest light extinction with σ_{sp} = 181 ± 82 Mm^{-1}, σ_{ap} = 12.1 ± 6.4 Mm^{-1}. Dust-dominated aerosols had substantial contributions from both super micrometer and submicrometer D_p particles (sf = 0.45), and though not hydrophobic were the least hygroscopic and showed deliquescent behavior.

[43]   The foremost feature of the North Pacific aerosol was the prevalence and importance to light scattering resulting from deliquescence, crystallization, hysteresis, and the existence of metastable droplets. For the four air mass categories of marine, polluted, dust, and volcanic considered here, 88%, 54%, 75%, and 0% of the individual f(RH) curves with D_p < 10 μm, respectively, were deliquescent. The deliquescence and crystallization RH (DRH and CRH) were 77 ± 2% and 42 ± 3%, respectively, and they ranged from 74% < DRH < 80% and 40% < CRH < 44%. The ambient aerosol was primarily on the upper branch or intermediate to the two branches of the hysteresis loop for marine and polluted cases (98% and 88%, respectively) and

Table 7. Curve Fit Parameters for Single Scattering Albedo Using a Fourth-Order Polynomial Curve Fit ($\omega(RH) = \nu RH^4 + wRH^3 + xRH^2 + yRH + z$) at $\lambda = 550$ nm for Size Cuts of D_p <10 μm and 1 μm for Marine, Polluted, Volcanic, and Dust-Influenced Air Masses[a]

	ν	w	x	y	z	R^2
ω(RH) (10 μm, 550 nm) Lower						
Marine	−2.515E−8	6.128E−6	−5.450E−4	2.123E−2	6.742E−1	0.960
Polluted	−5.421E−8	1.390E−5	−1.274E−3	5.030E−2	1.791E−1	0.976
Volcanic	−7.279E−9	2.188E−6	−2.244E−4	1.059E−2	7.205E−1	0.998
Dust	−2.321E−8	6.151E−6	−5.675E−4	2.194E−2	6.325E−1	0.936
ω(RH) (10 μm, 550 nm) Upper						
Marine	−5.909E−9	1.685E−6	−1.753E−4	8.038E−3	8.503E−1	0.984
Polluted	8.095E−9	−1.457E−6	9.441E−5	−1.803E−3	9.059E−1	0.999
Volcanic	−4.329E−8	1.091E−5	−1.006E−3	4.124E−2	2.781E−1	0.996
Dust	9.765E−10	−1.187E−7	9.188E−6	−2.343E−4	9.362E−1	0.996
ω(RH) (1 μm, 550 nm) Lower						
Marine	−1.005E−7	2.400E−5	−2.074E−3	7.787E−2	−1.484E−1	0.943
Polluted	−5.699E−8	1.458E−5	−1.318E−3	5.124E−2	1.407E−1	0.978
Volcanic	−2.078E−8	5.642E−6	−5.436E−4	2.332E−2	5.268E−1	0.998
Dust	−3.686E−8	9.418E−6	−8.245E−4	2.975E−2	5.232E−1	0.922
ω(RH) (1 μm, 550 nm) Upper						
Marine	−1.666E−9	7.973E−7	−1.128E−4	7.082E−3	7.894E−1	0.974
Polluted	−1.464E−8	4.352E−6	−4.459E−4	2.035E−2	5.353E−1	0.999
Volcanic	1.081E−8	−2.603E−6	2.373E−4	−8.298E−3	9.874E−1	0.998
Dust	−8.749E−9	2.047E−6	−1.609E−4	5.688E−3	8.253E−1	0.988

[a]Light absorption coefficient (σ_{ap}) is assumed independent of RH. Measurements occurred over the range 35% < RH < 85%.

Table 8. Curve Fit Parameters for Linear Fits for b(RH) ($\lambda = 550$ nm) and å(RH) ($\lambda = 450/550$ nm) for Marine, Polluted, Volcanic, and Dust-Influenced Air Masses[a]

	då/dRH	å (RH = 0%)	R^2	db/dRH	b (RH = 0%)	R^2
$D_p < 10\ \mu m$						
Marine	−0.0021	0.1829	0.0761	−0.0009	0.1388	0.7281
Polluted	−0.0007	1.2618	0.133	−0.0009	0.1572	0.9548
Volcanic	−0.0058	2.0672	0.8774	−0.0009	0.1474	0.9234
Dust	0.0037	0.5603	0.5745	−0.00055	0.1413	0.792
$D_p < 1\ \mu m$						
Marine	−0.0273	2.8167	0.8059	−0.0019	0.1995	0.7237
Polluted	−0.0092	2.3891	0.8877	−0.0015	0.1717	0.9356
Volcanic	0.0003	1.4139	0.0117	−0.0011	0.1588	0.8949
Dust	−0.0085	2.4854	0.8866	−0.00075	0.1535	0.8221

[a]Measurements occurred over the range 35% < RH < 85%.

on the lower branch or intermediate for the dust cases (100%). The importance of hysteresis to aerosol radiative effects is shown by the ratios of f(RH) between the upper and lower branches of the hysteresis loop (h(RH)) and on average h(RH∼60%) was 1.6, 1.3, and 1.25 for marine, polluted, and dust aerosols. Knowing the hydration state of the ambient aerosol, the ambient RH, and the hysteresis loop, f(RH = ambient) was calculated and was observed to depend strongly on the aerosol hygroscopicity, ambient RH, and aerosol hydration state. For the marine, polluted, dust and volcanic cases considered here, f(RH = ambient) was 2.56 ± 0.92, 1.86 ± 0.76, 1.25 ± 0.48, and 2.88 ± 0.92, respectively, though highly variable having a range of $1 < f$(RH = ambient) < 6.

[44] For all air mass types, light extinction was predominated by σ_{sp} as $\omega = 0.94 \pm 0.03$ for dust and polluted periods to 0.99 ± 0.01 for marine aerosols at ambient RH, with intermediate ω values for volcanic influenced periods. The most pronounced humidity effects on ω were observed for polluted aerosols with ω increasing from 0.91 to 0.96 as RH increased from 40 to 85% and showed a difference of 0.02 between ω on the upper and lower branches of the hysteresis loop in the range 60% < RH < 70%. Though no systematic differences in hemispheric backscatter fraction were observed for dry conditions, b at ambient RH ranged from 0.069 ± 0.022 to 0.111 ± 0.019 for dust and volcanic aerosols, respectively, and intermediate for marine and polluted. This was a result of ambient RH differences as the RH influence on b was substantial with b decreasing from 0.11 to 0.06 for marine air masses and similarly for the other cases. The wavelength dependence of σ_{sp} as characterized by the Ångström exponent at ambient RH showed a small dependence on RH though large differences with aerosol type with average values ranging from å = 0.16 ± 0.60 for marine to 1.49 ± 0.29 for volcanic aerosols, with polluted and dust aerosols intermediate. These measurements contribute to characterizing aerosol optical properties for mixtures of important, diverse aerosol types including marine, polluted, volcanic, and dust aerosols and are available for use in climate models.

References

Anderson, T. L., and J. A. Ogren, Determining aerosol radiative properties using the TSI 3563 integrating nephelometer, *Aerosol Sci. Technol.*, *29*, 57–69, 1998.

Anderson, T. L., et al., Performance characteristics of a high sensitivity, three wavelength, total scatter/backscatter nephelometer, *J. Atmos. Oceanic Technol.*, *13*(5), 967–986, 1996.

Ångström, A., Parameters of Atmospheric Turbidity, *Tellus*, *16*, 64–75, 1964.

Bates, T. S., D. J. Coffman, D. S. Covert, and P. K. Quinn, Regional marine boundary layer aerosol size distributions in the Indian, Atlantic, and Pacific Oceans: A comparison of INDOEX measurements with ACE-1, ACE-2, and Aerosols99, *J. Geophys. Res.*, *107*(D19), 8026, doi:10.1029/2001JD001174, 2002.

Bergin, M. H., J. A. Ogren, S. E. Schwartz, and L. M. McInnes, Evaporation of ammonium nitrate aerosol in a heated nephelometer: Implications for field measurements, *Environ. Sci. Technol.*, *31*(10), 2878–2883, 1997.

Bohren, C. F., and D. R. Huffman, *Absorption and Scattering of Light by Small Particles*, 530 pp., John Wiley, Hoboken, N. J., 1983.

Bond, T. C., T. L. Anderson, and D. Campbell, Calibration and intercomparison of filter based measurements of visible light absorption by aerosols, *Aerosol Sci. Technol.*, *30*, 582–600, 1999.

Boucher, O., and T. L. Anderson, General circulation model assessment of the sensitivity of direct climate forcing by anthropogenic sulfate aerosols to aerosol size and chemistry, *J. Geophys. Res.*, *100*(D12), 26,117–26,134, 1995.

Carrico, C. M., M. J. Rood, and J. A. Ogren, Aerosol light scattering properties at Cape Grim, Tasmania, during the First Aerosol Characterization Experiment (ACE 1), *J. Geophys. Res.*, *103*(D13), 16,565–16,574, 1998.

Carrico, C. M., M. J. Rood, J. A. Ogren, C. Neusüß, A. Wiedensohler, and J. Heintzenberg, Aerosol optical properties at Sagres, Portugal, during ACE 2, *Tellus, Ser. B*, *52*, 694–716, 2000.

Chameides, W. L., and A. W. Stelson, Aqueous-phase chemical processes in deliquescent sea salt aerosols: A mechanism that couples the atmospheric cycles of S and sea salt, *J. Geophys. Res.*, *97*, 20,525–20,580, 1992.

Chameides, W. L., et al., Case study of the effects of atmospheric aerosols and regional haze on agriculture: An opportunity to enhance crop yields in China through emission controls, *Proc. Nat. Acad. Sci.*, *96*(24), 13,626–13,633, 1999.

Charlson, R. J., S. E. Schwartz, J. M. Hales, R. D. Cess, J. A. Coakley Jr., J. E. Hansen, and D. J. Hofmann, Climate forcing by anthropogenic aerosols, *Science*, *255*, 423–430, 1992.

Covert, D. S., R. J. Charlson, and N. C. Ahlquist, A study of the relationship of chemical composition and humidity to light scattering by aerosols, *J. Appl. Meteorol.*, *11*(6), 968–976, 1972.

Cziczo, D. J., J. B. Nowak, J. H. Hu, and J. P. D. Abbatt, Infrared spectroscopy of model tropospheric aerosols as a function of relative humidity: Observation of deliquescence and crystallization, *J. Geophys. Res.*, *102*, 18,843–18,850, 1997.

Dentener, F. J., G. R. Carmichael, Y. Zhang, J. Lelieveld, and P. J. Crutzen, Role of mineral aerosol as a reactive surface in the global troposphere, *J. Geophys. Res.*, *101*, 22,869–22,889, 1996.

Hansson, H.-C., M. J. Rood, S. Koloutsou-Vakakis, K. Hämeri, D. Orsini, and A. Wiedensohler, NaCl aerosol particle hygroscopicity dependence on mixing with organic compounds, *J. Atmos. Chem.*, *31*, 321–346, 1998.

Heintzenberg, J., R. J. Charlson, A. D. Clarke, C. Liousse, V. Ramaswamy, K. P. Shine, M. Wendisch, and G. Helas, Measurements and modeling of aerosol single-scattering albedo: Progress, problems, and prospects, *Beitr. Phys. Atmos.*, *70*(4), 249–263, 1997.

Huebert, B. J., T. Bates, P. B. Russell, G. Shi, Y. J. Kim, K. Kawamura, G. Carmichael, and T. Nakajima, An overview of ACE-Asia: Strategies for quantifying the relationships between Asian aerosols and their climatic impacts, *J. Geophys. Res.*, *108*(D23), 8633, doi:10.1029/2003JD003550, in press, 2003.

Jaffe, D., et al., Transport of Asian air pollution to North America, *Geophys. Res. Lett.*, *26*, 711–714, 1999.

Kaufmann, Y. J., D. Tanré, and O. Boucher, A satellite view of aerosols in the climate system, *Nature*, *419*, 215–223, 2002.

Koloutsou-Vakakis, S., C. M. Carrico, P. Kus, M. J. Rood, Z. Li, R. Shrestha, J. A. Ogren, J. C. Chow, and J. G. Watson, Aerosol properties at a midlatitude Northern Hemisphere continental site, *J. Geophys. Res.*, *106*(D3), 3019–3032, 2001.

Kotchenruther, R. A., P. V. Hobbs, and D. A. Hegg, Humidification factors for atmospheric aerosols off the mid-Atlantic coast of the United States, *J. Geophys. Res.*, *104*(D2), 2239–2251, 1999.

Lelieveld, J., et al., The Indian Ocean Experiment: Widespread air pollution from south and southeast Asia, *Science*, *291*(5506), 1031–1036, 2001.

Li-Jones, X., H. B. Maring, and J. M. Prospero, Effect of relative humidity on light scattering by mineral dust as measured in the marine boundary layer over the tropical Atlantic Ocean, *J. Geophys. Res.*, *103*(D23), 31,113–31,121, 1998.

Marshall, S. F., D. S. Covert, and R. J. Charlson, Relationship between asymmetry factor and backscatter ratio: Implications for aerosol climate forcing, *Appl. Opt.*, *34*, 6306–6311, 1995.

O'Dowd, C. D., M. H. Smith, I. E. Consterdine, and J. A. Lowe, Marine aerosol, sea-salt, and the marine sulphur cycle: A short review, *Atmos. Environ.*, *31*(1), 73–80, 1997.

Pilinis, C., S. N. Pandis, and J. H. Seinfeld, Sensitivity of a direct climate forcing by atmospheric aerosols to aerosol size and composition, *J. Geophys. Res.*, *100*(D9), 18,739–18,754, 1995.

Ramanathan, V., P. J. Crutzen, J. T. Kiehl, and D. Rosenfeld, Atmosphere-Aerosols, climate, and the hydrological cycle, *Science*, *294*(5549), 2119–2124, 2001.

Robock, A., Volcanic eruptions and climate, *Rev. Geophys.*, *38*(2), 191–219, 2000.

Rood, M. J., M. A. Shaw, T. V. Larson, and D. S. Covert, Ubiquitous nature of ambient metastable aerosol, *Nature*, *337*(6207), 537–539, 1989.

Russell, P. B., et al., Comparison of aerosol single scattering albedos derived by diverse techniques in two North Atlantic experiments, *J. Atmos. Sci.*, *59*(3), 609–619, 2002.

Shaw, M. A., and M. J. Rood, Measurement of the crystallization humidities of ambient aerosol particles, *Atmos. Environ., Part A*, *24*(7), 1837–1841, 1990.

Sokolik, I. N., and O. B. Toon, Direct radiative forcing by anthropogenic airborne mineral aerosols, *Nature*, *381*, 681–683, 1996.

Song, C. H., and G. R. Carmichael, A three dimensional modeling investigation of the evolution processes of dust and sea-salt particles in East Asia, *J. Geophys. Res.*, *106*(D16), 18,131–18,154, 2001.

Tang, I. N., Chemical and size effects of hygroscopic aerosols on light scattering coefficients, *J. Geophys. Res.*, *101*(D14), 19,245–19,250, 1996.

Tang, I. N., and H. R. Munkelwitz, Composition and temperature dependence of the deliquescence properties of hygroscopic aerosols, *Atmos. Environ., Part A*, *27*(4), 467–473, 1993.

Tang, I. N., K. H. Fung, D. G. Imre, and H. R. Munkelwitz, Phase transformation and metastability of hygroscopic microparticles, *Aerosol Sci. Technol.*, *23*, 443–453, 1995.

Tang, I. N., A. C. Tridico, and K. H. Fung, Thermodynamic and optical properties of sea salt aerosols, *J. Geophys. Res.*, *102*(D19), 23,269–23,275, 1997.

ten Brink, H. M., A. Khlystov, G. P. A. Kos, T. Tuch, C. Roth, and W. Kreyling, A high flow humidograph for testing the water uptake by ambient aerosol, *Atmos. Environ.*, *34*, 4291–4300, 2000.

Winter, B., and P. Chýlek, Contribution of sea salt aerosol to the planetary clear-sky albedo, *Tellus, Ser. B*, *49*, 72–79, 1997.

Wolf, M. E., and G. M. Hidy, Aerosols and climate: Anthropogenic emissions and trends for 50 years, *J. Geophys. Res.*, *102*(D10), 11,113–11,121, 1997.

Xu, J., M. H. Bergin, X. Yu, G. Liu, J. Zhao, C. M. Carrico, and K. Baumann, Measurement of aerosol chemical, physical and radiative properties in the Yangtze delta region of China, *Atmos. Environ.*, *36*(2), 161–173, 2002.

T. S. Bates and P. K. Quinn, Pacific Marine Environmental Laboratory, National Oceanic and Atmospheric Administration, Seattle, WA 98115, USA. (tim.bates@noaa.gov; patricia.k.quinn@noaa.gov)

C. M. Carrico, Department of Atmospheric Science, Colorado State University, Fort Collins, CO 82523-1371, USA. (carrico@lamar.colostate.edu)

P. Kus and M. J. Rood, Department of Civil and Environmental Engineering, University of Illinois, Urbana, IL 61801, USA. (pinarkus@uiuc.edu; mrood@uiuc.edu)